

THE UNIVERSITY OF MICHIGAN

COLLEGE OF ENGINEERING

Department of Electrical Engineering

Cooley Electronics Laboratory

This project was undertaken in collaboration with the Countermeasures Department of the Institute of Science and Technology, The University of Michigan. The experimental work of this project has been done in the Countermeasures Laboratories facility.

Interim Technical Report No. 2

4957-2-P

Period Covering May 1, 1962 to August 1, 1962

DERIVATION OF AEROSPACE ANTENNA

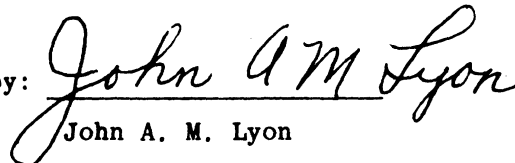
COUPLING FACTOR INTERFERENCE

PREDICTION TECHNIQUES

D. K. Adams  
W. R. DeHart  
R. B. Harris

Y. K. Kwon  
R. E. Kovac  
A. I. Simanyi

Approved by:

  
John A. M. Lyon

Under Contract With United States Air Force  
AIR FORCE SYSTEMS COMMAND  
AERONAUTICAL SYSTEMS DIVISION  
Contract No. AF 33(657)-8178  
Wright-Patterson Air Force Base, Ohio

Administered Through

Office of Research Administration

Ann Arbor

September 1962

4957-2-P = RL-2120

TABLE OF CONTENTS

	<u>Page</u>
LIST OF ILLUSTRATIONS	111
1. REPORTS, TRAVEL, AND VISITORS	1
2. SUMMARY	1
3. ACTIVITIES FOR THE NEXT PERIOD	2
4. DETAILED RESULTS	5
4.1. ANALYSIS AND DESIGN	5
4.1.1. THEORETICAL ANALYSIS OF SLOT COUPLING	5
4.1.2. EDGE-TO-EDGE SLOT COUPLING	15
4.1.3. SPIRAL ANTENNA	15
4.2. EXPERIMENTAL STUDIES	23
4.2.1. SLOT COUPLING MEASUREMENTS	23
4.2.2. WAVEGUIDE-TO-MONOPOLE TRANSFORMER CHARACTERISTICS	50
APPENDIX	55
REFERENCES	62

LIST OF ILLUSTRATIONS

<u>Figure</u>	<u>Title</u>	<u>Page</u>
1	Waveguide Coupled to Half-Space	6
2	Slot Coordinates	11
3	Slot Geometry	14
4	Comparison of Theoretical and Experimental Slot Coupling Results	16
5	Comparison of Theoretical and Experimental Slot Coupling Results	17
6	Coaxial Balun for Out-of-Phase Excitation	20
7	Cavity and Spiral Feed	22
8	Ground Plane Used for Measurement of Edge Effects	25
9	Absorbent Shield	26
10	Two Arbitrarily Oriented Slots	28
11	Slot Layout for Preliminary Coupling Measurements	28
12	New Ground Plane with Rotatable Slot	30
13	Mechanical Detail of Rotatable Slot	31
14	VSWR of Rotary Joints versus Frequency	34
15	Rotary Joint Connecting Arms	34
16	Methods of Klystron Amplitude Modulation	36
17	Modified Microwave Bridge	38
18	Final Layout of Revised Microwave Bridge	46
19	Slot Coupling Phase Relationships	47
20	Slot Waveguide Assembly with Tuned Screws	47
21	Smith Diagram for Slot Waveguide Assembly	49
22	VSWR of Slot Waveguide Assembly versus Phase Shift of Short Section	51

LIST OF ILLUSTRATIONS (continued)

<u>Figure</u>	<u>Title</u>	<u>Page</u>
23	VSWR of Waveguide-to-Monopole Transformer Loaded with Monopole (resonant at 2.81 mc/s.)	53
24	Optimum Frequency versus Monopole Height	54
25	Range of Integration for $\mu$ and $\lambda$	58
26	Range of Integration for $\nu$ and $\sigma$	58

## 1. REPORTS, TRAVEL, AND VISITORS

On May 3, 1962, project personnel visited Wright-Patterson Air Force Base, Ohio. Details of this visit are included in the previous Interim Technical Report Number 1 dated June 1962.

## 2. SUMMARY

The analytical work previously reported in the first quarterly report has been continued. The power coupling between slots in a broadside-to-broadside arrangement was determined to be about 20 db below unity coupling for a spacing of one wavelength between the centers of the slots and to decrease at a rate of about 6 db per octave for spacings greater than one wavelength. For the edge-to-edge slot arrangement, the power coupling between slots was about 31.5 db below unity coupling at a spacing of one wavelength and decreased at a rate of about 12 db per octave for spacings greater than one wavelength. These coupling factors were determined both theoretically and experimentally with very good agreement. This type of simplified analysis has been extended to angular arrangements of rectangular slots. The analysis has been sufficiently developed so that it is now possible to predict within one db the power interference coupling between two rectangular slots at any orientation.

Experimental procedures were followed in determining the power interference coupling between two slots at any angular orientation. Details of the physical arrangements as well as the modified bridge for measurement are described in Section 4.2.1.

The experimental determination of the phase associated with the power interference coupling between two rectangular slots has been somewhat

troublesome. The reliability of such measurements has not been good. For this reason substantial time has been devoted to the improvement of the phase measurement procedures. Since the improved measurement network has just been finished, complete information on phase is not available at this writing. However, it now appears that the phase angular measurements can be made with a reliability of plus or minus five electrical degrees.

Preliminary monopole impedance studies were continued. A monopole together with a ridge transformer has now been completely designed and tested. The impedance of the monopole at the junction with the ridge is 33.83 ohms. Two of these monopole units have now been fabricated and are available for coupling measurements.

### 3. ACTIVITIES FOR THE NEXT PERIOD

Within the first half of the next quarterly period slot coupling measurements of both amplitude and phase shall have been made for all arrangements of rectangular slots in a flat plate. This is on the basis that extended arrangements of slots can be predicted by either two-slot analysis or two-slot measurements.

Currently analytical studies for slots in a conducting plane are being successfully concluded. Not much more time on this aspect of the project is now contemplated.

A cavity-backed Archimedean spiral together with a balun transformer feed has now been fabricated. Input characteristics are being measured. Initially it appears that a minimum of three spirals will be needed. Two spirals will have the same rotation of circular polarization. Then one of these spirals will be paired with a second spiral which has an opposing

rotation of polarization. Measurements will be made at first on these two combinations. For reference purposes it is considered desirable to study the air coupling between two spirals without any conducting ground plane. However, it is recognized that terminal considerations may drastically influence the results obtained for this air coupling. Even though the reliability of such data may be poor it is anticipated that attempts will be made to get some data of this type.

In general, two spirals will be studied with conducting ground plane coupling present. This means that the ground plane will have circular openings sufficient to accommodate the cavity-backed spirals. It is anticipated that power interference coupling in the far zone will be independent of the angular orientation of a spiral. However, when two spirals are in close proximity this may not be the situation.

It may be desirable to study two spirals set in a dielectric plane. This could be considered an intermediate case of the two previously described and might indicate the relative importance of dielectric and conducting materials in the coupling phenomena.

A further possible arrangement of large numbers of spirals would be to have an orderly arrangement of spirals printed by photo-etching process on a sheet of dielectric material. Such a sheet could then be backed by a large conducting ground plane. The sheet itself would be between the metal deposited spiral elements and the conducting ground plane. If necessary an additional sheet of dielectric material could be inserted between the printed sheet and the conducting ground plane. This does not place the spirals in the ground plane, but somewhat in front of the ground plane.

The measurements on spiral elements can be made at the same time as the measurements on slot couplings. This means that the measuring equipment

used on one of these will not be needed for the measurements on the other. However, in going to monopole coupling measurements it is anticipated that substantial equipment which was used for slot coupling will now be used for monopole coupling. For this reason measurements on monopoles have been deferred until all slot coupling measurements in a conducting ground plane have been accomplished.

Theoretical analysis of the coupling of two spirals is now underway. In a preliminary fashion in this analysis, various simplified representations of the spiral are being considered. However, it is hoped to make a reasonably rigorous study of the spiral antenna and the power interference coupling of one such antenna to another. Like and opposite rotations of polarization are being considered.

Immediately after coupling measurements on monopoles have been concluded it is anticipated that slot coupling measurements with slots mounted in cylindrical surfaces will be considered. It is proposed that the arrangements of slots in the cylindrical surface will be limited to either the axial orientation or circumferential orientation. In other words, it is not contemplated at this time to use all angles of orientation of two slots on the cylindrical surface. It is believed that this restricted testing program will supply much needed information not hitherto available. Furthermore, such experimental results would have some chance of being proved out by analysis.

Theoretical analysis of slots in cylindrical conducting surfaces will be made. This type of analysis will commence as soon as substantial analysis has been established for the spiral coupling cases.

No substantial analysis on monopole coupling is being contemplated. On this research project, use has been made of previous analysis and design



data in order to establish monopoles for use as antenna elements offering the theoretical driving point impedance. The whole purpose of the study of monopole coupling in this program is to present a comparison of this series of power interference coupling studies with other such studies which have gone on before and which are being carried forward at the present time by various research groups.

#### 4. DETAILED RESULTS

##### 4.1. ANALYSIS AND DESIGN

The coupling between two fundamental half-wave resonant slots was determined analytically by use of far field approximations for the magnetic coupling field components. In this derivation, the coupling between slots can be determined for any orientation of one slot with respect to the other slot, except for end-to-end slot coupling. In this case near-field approximations for the coupling fields are required.

A spiral antenna has been constructed to be used in making spiral antenna coupling measurements at L-band.

4.1.1. THEORETICAL EVALUATION OF SLOT COUPLING. In the analysis of coupling of the waveguide-fed slot antennas in an infinite ground plane, the accurate field patterns of one slot antenna must be known. Consider a rectangular waveguide coupled to half-space as shown in Figure 1. Let the interior of the waveguide represent region 1 and the half-space represent region 2. Assume that (a) the waveguide walls and the ground plane are perfectly conducting and have negligible thickness, and (b) the ground plane is infinite so that no radiation field exists behind the ground plane or outside the guide.

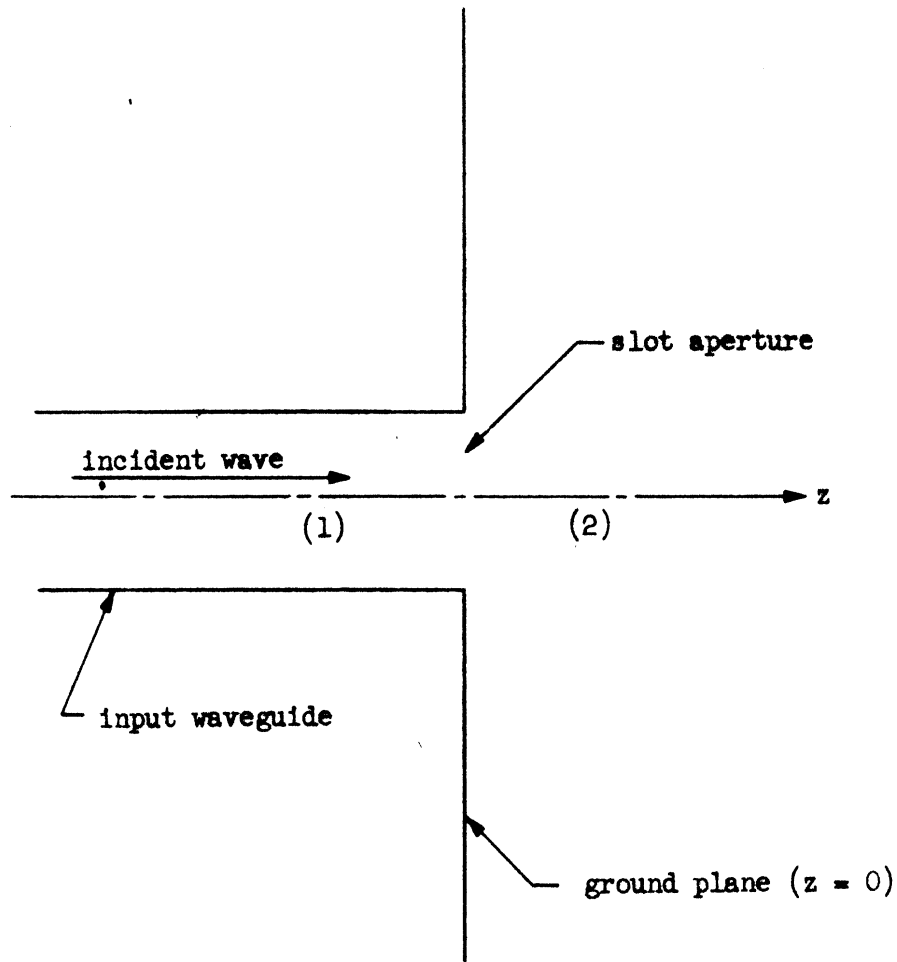


Figure 1. Waveguide Coupled to Half-Space

The electromagnetic field can be represented everywhere by the Hertzian magnetic vector  $\vec{\pi}^*$  from which the electric and magnetic fields  $\vec{E}$  and  $\vec{H}$  are derived through the relations from Reference 1,

$$\vec{E} = -\mu \nabla \times \frac{\partial \vec{\pi}^*}{\partial t}, \quad (1)$$

and

$$\vec{H} = \nabla \nabla \cdot \vec{\pi}^* - \mu \epsilon \frac{\partial^2 \vec{\pi}^*}{\partial t^2}. \quad (2)$$

where  $\epsilon$  is the dielectric permittivity and  $\mu$  is the magnetic permeability. Assume harmonic time-variation  $\exp(j\omega t)$ , where  $\omega$  is the angular frequency. Equations (1) and (2) become

$$\vec{E} = -j\omega\mu\nabla\times\vec{\pi}^*, \quad (3)$$

and

$$\vec{H} = \nabla\nabla\cdot\vec{\pi}^* + k^2\vec{\pi}^*, \quad (4)$$

where  $k^2 = \omega^2\mu\epsilon$ .

According to a fundamental existence theorem of electromagnetic field theory, an uniquely determined electromagnetic field exists provided the tangential component of either the electric field or the magnetic field is specified at each point (including discontinuity points) of the surface bounding the given region. For the present problem the tangential electric field  $\vec{E} \times \hat{n}$  vanishes on the ground plane and along the infinite hemisphere centered about the origin (radiation condition), and it has the value  $\vec{M}$  in the slot. The unit vector  $\hat{n}$  normal to the bounding surfaces points into the half-space. The exciting field in the slot is equivalent to a magnetic surface current of density  $\vec{M}$  on a conductor. By employing the duality of the electric current and magnetic current, the Hertzian magnetic vector is obtained in the form:

$$\vec{\pi}^* = \frac{2}{4\pi j\omega\mu} \int_{\text{slot}} \vec{M}(\vec{r}') \frac{e^{-jk|\vec{r} - \vec{r}'|}}{|\vec{r} - \vec{r}'|} dS', \quad (5)$$

where  $\vec{r}$  denotes the field point, and

$\vec{r}'$  denotes the position vector of the magnetic current element.

The factor of two results from the imaging effect (see Reference 3).

Substituting Equation (5) into Equation (4),

$$\vec{H}(\vec{r}) = \frac{-j\omega\epsilon}{2\pi} \int_{\text{slot}} \left( \vec{I} + \frac{\nabla\nabla}{k^2} \right) \cdot \vec{M}(\vec{r}') \frac{e^{-jk|\vec{r} - \vec{r}'|}}{|\vec{r} - \vec{r}'|} dS' \quad (6)$$

where  $\vec{I}$  is the unit dyadic (therefore  $\vec{I} \cdot \vec{A} = \vec{A}$  and  $\vec{I} = \vec{A}$  for an arbitrary vector  $\vec{A}$ ). Since  $\vec{M} = \vec{E} \times \hat{n} = \vec{E} \times \hat{z}_0$ , where  $\hat{z}_0$  is the unit vector in the positive direction of the z-coordinate, then

$$\vec{H}(\vec{r}) = \int_{\text{slot}} \vec{Y}_h(\vec{r}, \vec{r}') \cdot \left[ \hat{z}_0 \times \vec{E}(\vec{r}') \right] dS', \quad (7)$$

where

$$\vec{Y}_h(\vec{r}, \vec{r}') = \vec{Y}_h(\vec{r}'; \vec{r}) = \frac{j\omega\epsilon}{2\pi} \left( \vec{I} + \frac{\nabla\nabla}{k^2} \right) \frac{e^{-jk|\vec{r} - \vec{r}'|}}{|\vec{r} - \vec{r}'|} \quad (8)$$

Equation (7) gives the magnetic field in the half-space if the electric field  $\vec{E}(\vec{r}')$  in the slot is known. The slot field  $\vec{E}(\vec{r}')$  can be determined, at least in theory, by imposing the condition that all components of  $\vec{E}$  and  $\vec{H}$  must be continuous in crossing from region 1 to region 2 (the determination of the field in the guide region is well known). However, this procedure leads to an integral equation which is not generally solvable. Therefore, assume that the slot field is the same as that of the  $TE_{10}$  mode of rectangular guide, namely:

$$\vec{E}(\vec{r}') = \vec{E}(t, \eta, 0) = \hat{x}_0 E_0 \cos \frac{\pi y}{b} \quad (9)$$

for  $-\frac{a}{2} < x < \frac{a}{2}$  and  $-\frac{b}{2} < y < \frac{b}{2}$ ,

where  $a$  = smaller dimension of the waveguide,

$b$  = larger dimension of the waveguide, and

$\hat{x}_0$  = unit vector in the positive direction of the x-coordinate  
(see Figure 2).

Substituting Equation (9) into Equation (7),

$$\vec{H}(\vec{r}) = E_0 \int_{\text{slot}} \vec{Y}_h(\vec{r}, \vec{r}') \cdot \hat{y}_0 \cos \frac{\pi y'}{b} dS', \quad (10)$$

where  $\hat{y}_0$  = unit vector in the positive direction of the y-coordinate.

Hence,

$$H_x = \frac{jE_0}{2\pi\omega\mu} \int_{-\frac{a}{2}}^{\frac{a}{2}} dx' \int_{-\frac{b}{2}}^{\frac{b}{2}} dy' \cos \frac{\pi y'}{b} \frac{\partial^2}{\partial x \partial y} \left( \frac{e^{-jk|\vec{r} - \vec{r}'|}}{|\vec{r} - \vec{r}'|} \right) \quad (11)$$

and

$$H_y = \frac{jE_0}{2\pi\omega\mu} \int_{-\frac{a}{2}}^{\frac{a}{2}} dx' \int_{-\frac{b}{2}}^{\frac{b}{2}} dy' \cos \frac{\pi y'}{b} \left( k^2 + \frac{\partial^2}{\partial y^2} \right) \left( \frac{e^{-jk|\vec{r} - \vec{r}'|}}{|\vec{r} - \vec{r}'|} \right) \quad (12)$$

After differentiation, the following assumptions are made in order to simplify the integration:

$$|\vec{r} - \vec{r}'| = \sqrt{(x - x')^2 + (y - y')^2 + z^2} \approx r - \frac{xx' + yy'}{r} \quad (13)$$

where  $r = \sqrt{x^2 + y^2 + z^2}$  ;

and

$$\frac{1}{|\vec{r} - \vec{r}'|} \approx \frac{1}{r}. \quad (14)$$

These assumptions are valid as long as any linear dimension of the slot is much smaller than  $|\bar{r} - \bar{r}'|$ . The results of the integration of Equations (11) and (12), after taking into account the assumptions of Equations (13) and (14), are:

$$H_x = -2j\omega\epsilon E_0 \frac{b}{\pi} \frac{e^{-jkr}}{kr} \left[ \frac{\sin\left(\frac{ka}{2} \sin\theta \cos\phi\right)}{\sin\theta \cos\phi} \right] \left[ \frac{\cos\left(\frac{kb}{2} \sin\theta \sin\phi\right)}{1 - \left(\frac{kb}{\pi}\right)^2 \sin^2\theta \sin^2\phi} \right] \sin^2\theta \sin\phi \cos\phi + O\left(\frac{1}{r^2}\right) \quad (15)$$

$$H_y = +2j\omega\epsilon E_0 \frac{b}{\pi} \frac{e^{-jkr}}{kr} \left[ \frac{\sin\left(\frac{ka}{2} \sin\theta \cos\phi\right)}{\sin\theta \cos\phi} \right] \left[ \frac{\cos\left(\frac{kb}{2} \sin\theta \sin\phi\right)}{1 - \left(\frac{kb}{\pi}\right)^2 \sin^2\theta \sin^2\phi} \right] (1 - \sin^2\theta \sin^2\phi) + O\left(\frac{1}{r^2}\right) \quad (16)$$

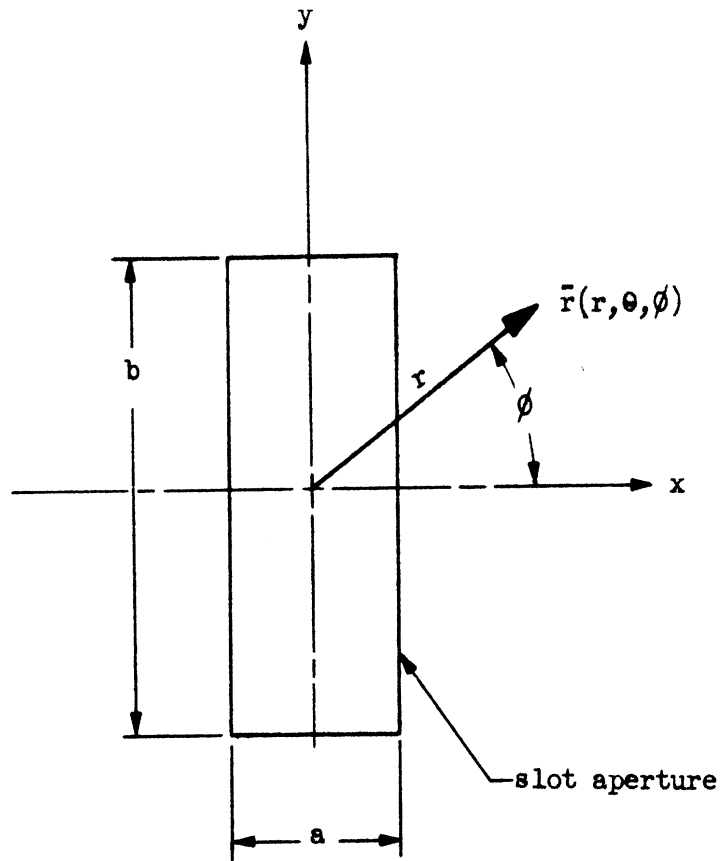
where  $O\left(\frac{1}{r^2}\right)$  means order of  $1/r^2$  and is negligible.

The power across a unit area is calculated from the expression:

$$P = \frac{1}{2} \operatorname{Re}(\bar{E} \times \bar{H}^*) = \frac{1}{2} \sqrt{\frac{\mu}{\epsilon}} |\bar{H}|^2. \quad (17)$$

The general form for the power per unit area for the slot problem is thus;

$$P_z = \frac{2\omega^2 \epsilon^2 b^2 E_0^2}{\pi^2 k^2 r^2} \sqrt{\frac{\mu}{\epsilon}} \left[ \frac{\sin\left(\frac{ka}{2} \sin\theta \cos\phi\right)}{\sin\theta \cos\phi} \right]^2 \left[ \frac{\cos\left(\frac{kb}{2} \sin\theta \sin\phi\right)}{1 - \left(\frac{kb}{\pi}\right)^2 \sin^2\theta \sin^2\phi} \right]^2 \left[ (\sin^2\theta \sin\phi \cos\phi)^2 + (1 - \sin^2\theta \sin^2\phi)^2 \right]. \quad (18)$$



Note: The z-axis positive direction is normal to the paper and toward the reader.

Figure 2. Slot Coordinates

On the ground plane ( $\theta = \frac{\pi}{2}$ ), the power per unit area can be written as

$$P_z = \frac{2\omega^2 \epsilon^2 b^2 E_0^2}{\pi^4 k^2 r^2} \sqrt{\frac{\mu}{\epsilon}} \sin^2\left(\frac{ka}{2} \cos \phi\right) \left[ \frac{\cos\left(\frac{kb}{2} \sin \phi\right)}{1 - \left(\frac{kb}{\pi}\right)^2 \sin^2 \phi} \right]^2 \quad (19)$$

The power transmitted from a slot is given by:

$$W = \frac{1}{2} \oint_{\text{slot}} \left[ \vec{E}(\vec{r}) \times \vec{H}^*(\vec{r}) \right] \cdot \hat{z}_0 \, dS. \quad (20)$$

Substituting  $\vec{E}(\vec{r}) = \hat{x}_o E_o \cos \frac{\pi y}{b}$  and Equation (10) for  $\vec{H}(\vec{r})$  into Equation (20),

$$W = \frac{1}{2} R_s \int_{\text{slot}} \left[ \int_{\text{slot}} \vec{Y}_h^*(\vec{r}, \vec{r}') \cdot \hat{y}_o E_o \cos \frac{\pi y'}{b} ds' \right] \cdot \hat{y}_o E_o \cos \frac{\pi y}{b} ds. \quad (21)$$

Integration of Equation (21) is done by using a method outlined in Reference 4 and is detailed in the Appendix (section 5). Hence,

$$W = \frac{8}{3\pi} \sqrt{\frac{\epsilon}{\mu}} \left(\frac{ab}{\lambda}\right)^2 E_o^2 F \quad (22)$$

where  $F = 1 - 0.374 \left(\frac{b}{\lambda}\right)^2 + 0.130 \left(\frac{b}{\lambda}\right)^4 - 0.154 \left(\frac{b}{\lambda}\right)^6$

$$- 1.36 \left(\frac{a}{\lambda}\right)^2 \left[ 1 - 0.268 \left(\frac{b}{\lambda}\right)^2 + 0.160 \left(\frac{b}{\lambda}\right)^4 \right] + 0.556 \left(\frac{a}{\lambda}\right)^4.$$

The gain of an antenna is given by:

$$g = \frac{4\pi r^2 P_r}{W_T} \quad (23)$$

where  $r$  = distance between the antenna and the point of observation,

$P_r$  = radial power density, and

$W_T$  = transmitted power.

For the problem at hand,  $P_r = P_z$  and  $W_T = 2W$  (since  $W$  is the power supplied by the slot and an equal amount of power is supplied by its image. Therefore, the gain of the half-space slot in this problem is given by

$$g = \frac{4\pi r^2 P_z}{2W} \quad (24)$$



Substituting Equations (19) and (22) in Equation (24), the gain of the slot is

$$g = \frac{3}{2} \left( \frac{\lambda}{\pi a} \right)^2 \frac{1}{F} \sin^2 \left( \frac{ka}{2} \cos \phi \right) \left[ \frac{\cos \left( \frac{kb}{2} \sin \phi \right)}{1 - \left( \frac{kb}{\pi} \right)^2 \sin^2 \phi} \right]^2 \quad (25)$$

The far-field coupling between one slot and another is defined by

$$C = \frac{W_R}{W_T} \quad (26)$$

where  $W_R$  is the power received by the second slot, and is given by

$$W_R = P_r A_R = P_r \left( \frac{g_R \lambda^2}{4\pi} \right), \quad (27)$$

where  $\lambda$  = free-space wavelength, and

$g_R$  = gain of the receiving slot.

Substituting Equations (23) and (27) into Equation (26) gives the coupling as

$$C = \left( \frac{\lambda}{4\pi r} \right)^2 g_T g_R, \quad (28)$$

where  $g_T$  is the gain of the transmitting slot. The gain of each slot is given by Equation (25). For a slot arrangement such as that shown in Figure 3, the far-field coupling is finally

$$C = \left( \frac{3\lambda^3}{8\pi^3 a_T a_R} \right)^2 \frac{1}{F_T F_R} \sin^2 \left( \frac{ka_T}{2} \cos \phi_T \right) \sin^2 \left( \frac{ka_R}{2} \cos \phi_R \right) \left[ \frac{\cos \left( \frac{kb_T}{2} \sin \phi_T \right)}{1 - \left( \frac{kb_T}{\pi} \right)^2 \sin^2 \phi_T} \right]^2 \left[ \frac{\cos \left( \frac{kb_R}{2} \sin \phi_R \right)}{1 - \left( \frac{kb_R}{\pi} \right)^2 \sin^2 \phi_R} \right]^2 \quad (29)$$

where  $a_T$  = smaller dimension of transmitting slot,

$a_R$  = smaller dimension of receiving slot,

$b_T$  = larger dimension of transmitting slot,

$b_R$  = larger dimension of receiving slot,

$\phi_T$  = orientation angle for transmitting slot,

$\phi_R$  = orientation angle for receiving slot,

$F_T = F | a = a_T, b = b_T, \text{ and}$

$F_R = F | a = a_R, b = b_R.$

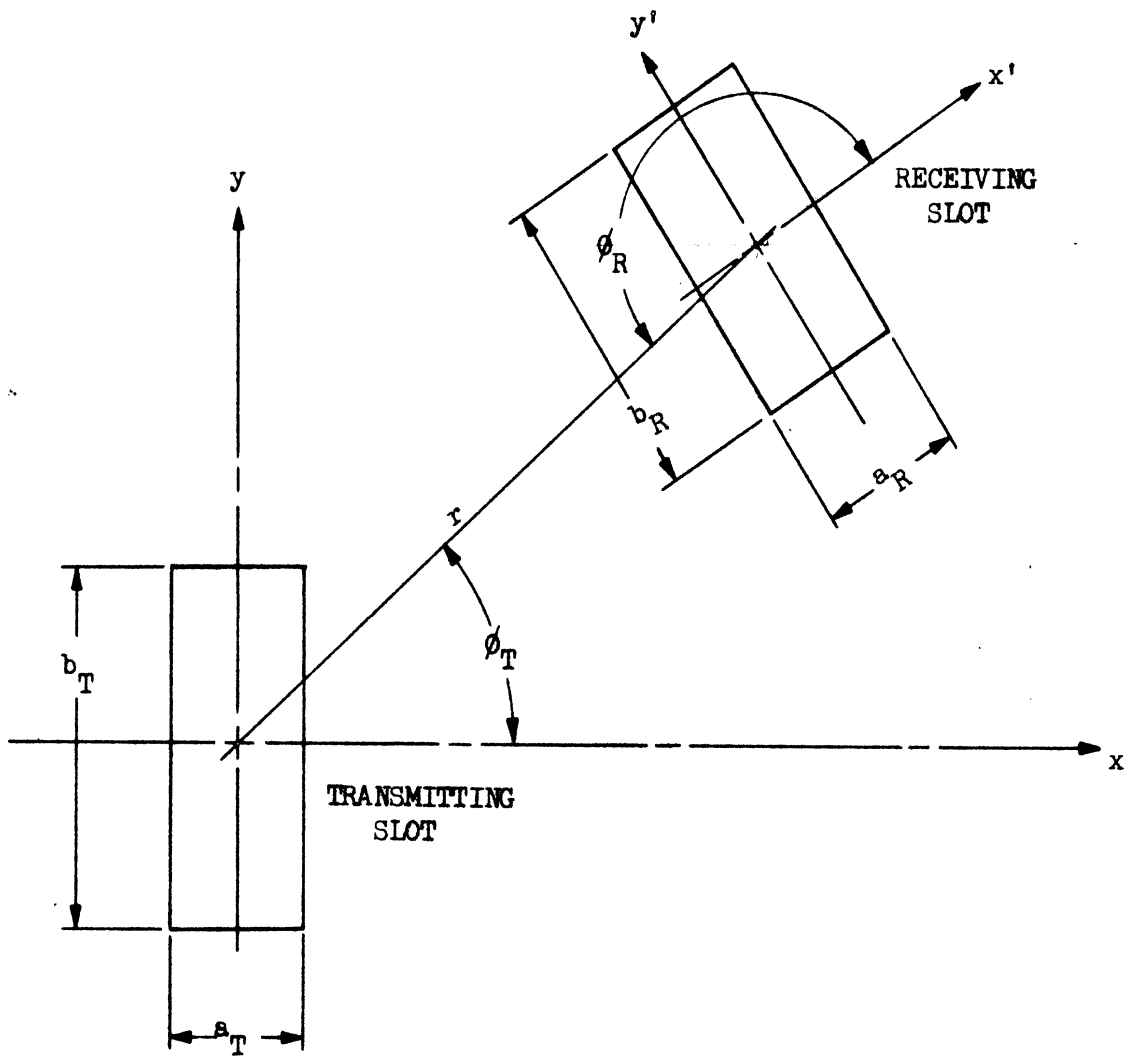


Figure 3. Slot Geometry

For this problem, i.e., two slots of equal apertures,

$$a_T = a_R = a \qquad b_T = b_R = b \qquad F_T = F_R = F$$

hence the coupling given by Equation (29) reduces to:

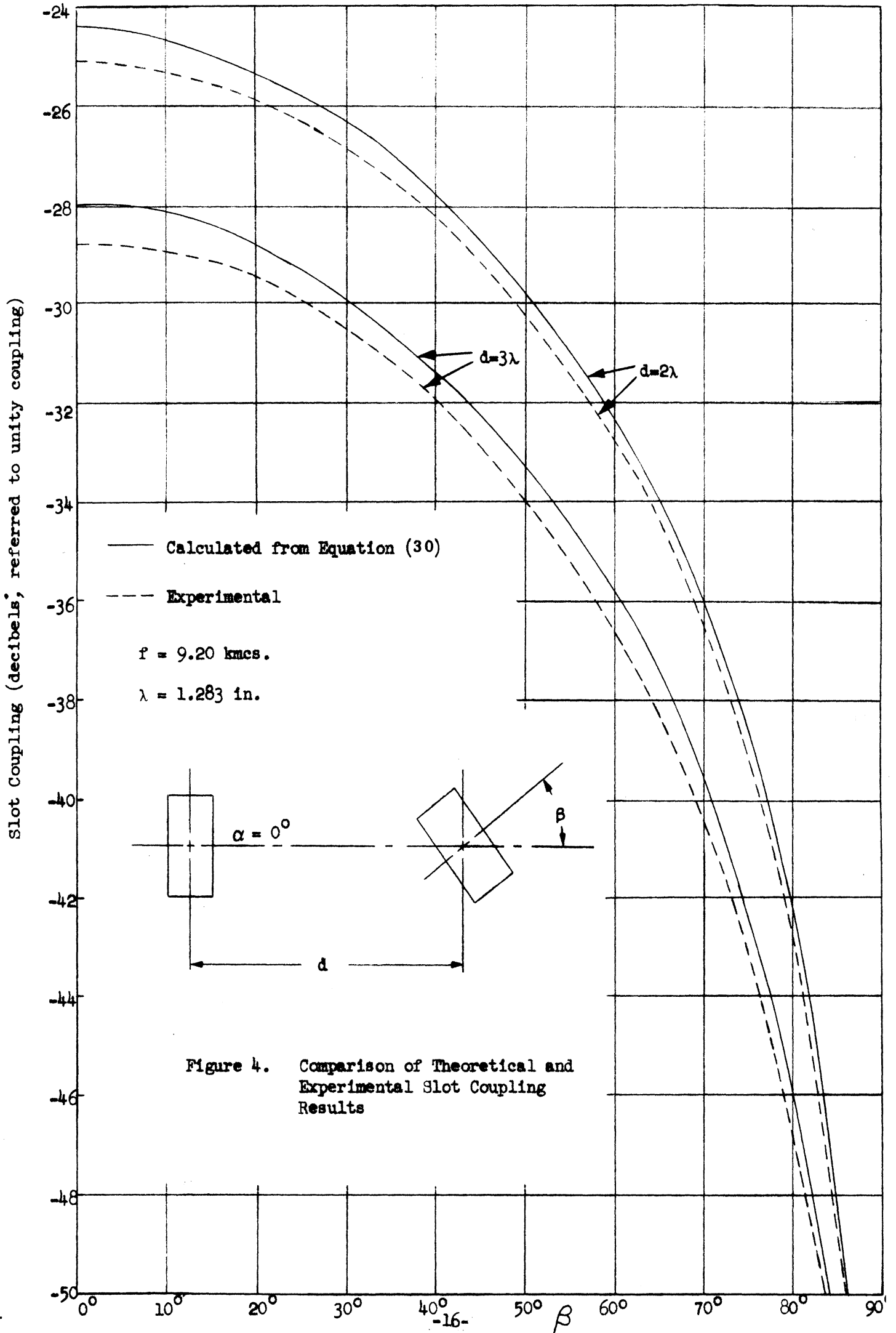
$$C = \left( \frac{3\lambda^3}{8\pi^3 a^2 r_F} \right)^2 \sin^2 \left( \frac{ka}{2} \cos \phi_T \right) \sin^2 \left( \frac{ka}{2} \cos \phi_R \right) \left[ \frac{\cos \left( \frac{kb}{2} \sin \phi_T \right)}{1 - \left( \frac{kb}{\pi} \right)^2 \sin^2 \phi_T} \right]^2 \left[ \frac{\cos \left( \frac{kb}{2} \sin \phi_R \right)}{1 - \left( \frac{kb}{\pi} \right)^2 \sin^2 \phi_R} \right]^2 \quad (30)$$

For  $a = 0.4''$ ,  $b = 0.9''$ , and  $\lambda = 1.283''$ , the far-field coupling given by Equation (30) for two situations are plotted in Figures 4 and 5. Experimental results are also shown for comparison.

4.1.2. **EDGE-TO-EDGE SLOT COUPLING.** Preliminary analytical derivation of the mathematical expressions for the coupling of slots oriented in an end-to-end configuration, which involves a near-field coupling phenomenon, has been made. However, improvement to the derivation is necessary before it can be reported.

#### 4.1.3. **SPIRAL ANTENNA.**

4.1.3.1. Resume of Spiral Antenna Characteristics. The basic properties of flat spiral antennas make them very useful in applications which require a broad-beamed, circularly polarized pattern that can be achieved across a wide frequency band (Reference 5). Various approximating solutions toward explaining the radiation pattern of two-arm spiral antennas have been proposed. The



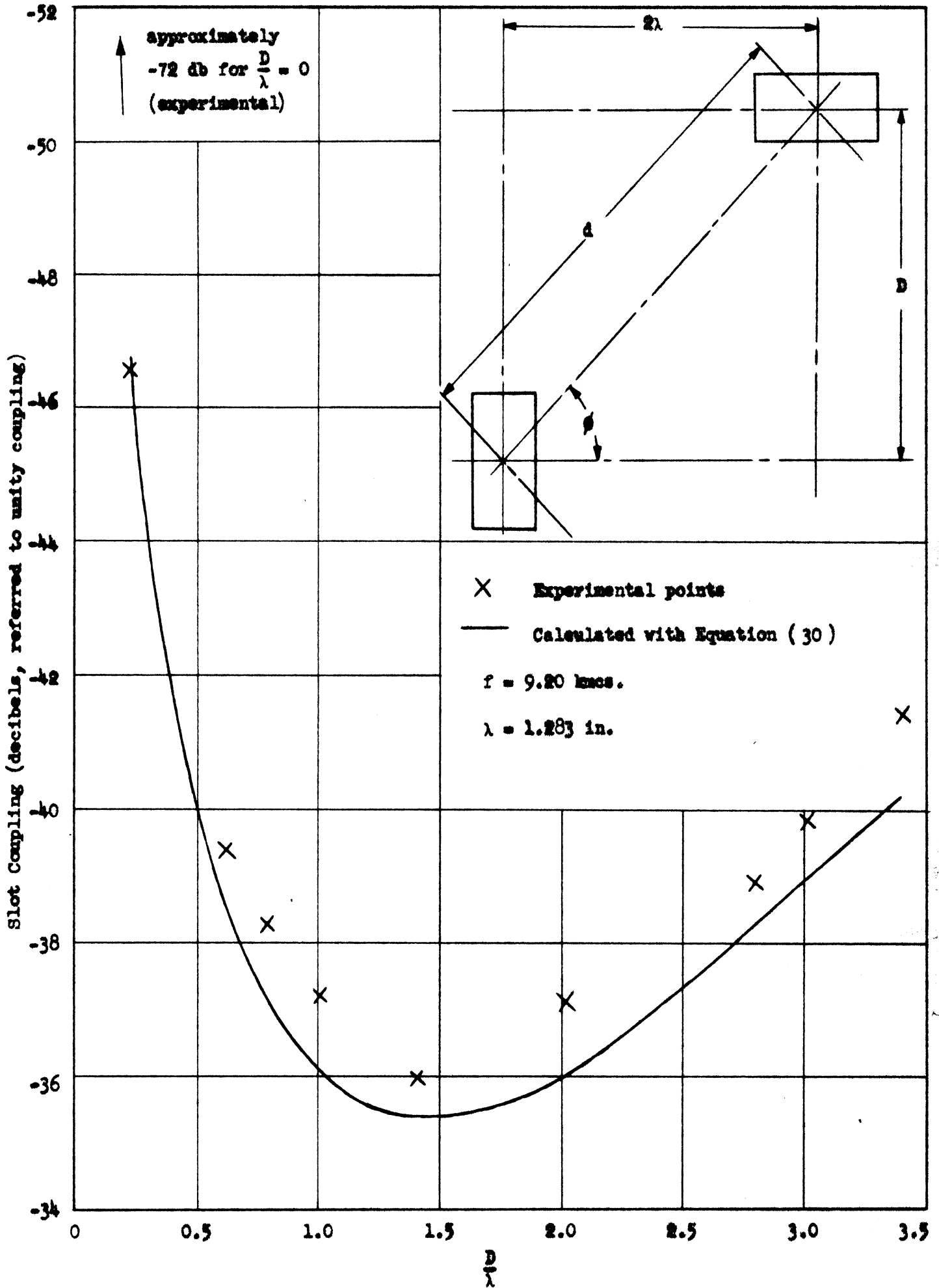


Figure 5. Comparison of Theoretical and Experimental Slot Coupling Results

so-called band theory provides a good method for understanding the operation of spirals (Reference 6). In short, this theory states that the chief contribution to the radiated energy for Archimedean spirals occurs from radiation bands which have a mean diameter of  $\lambda/\pi$ ,  $3\lambda/\pi$ , etc., for an out-of-phase excitation of the two spirals arms, and a mean diameter of  $2\lambda/\pi$ ,  $4\lambda/\pi$ , etc., for in-phase excitation of the arms. Kaiser (Reference 7) has presented some very illuminating diagrams of the computed phase shift along the spiral arms. From his presentation it is quite easy to see why radiation bands exist. For the out-of-phase excitation the current elements on adjacent portions of the two arms of the spiral at its input are 180 degrees apart. Since their physical separation is small in terms of wavelengths, the radiated fields cancel almost entirely. Proceeding outward along the spiral, the phases of the current elements on the two different arms approach each other due to the different line lengths traversed. Finally, at diameter  $d_0 = \lambda/\pi$ , adjacent current elements are in phase. Moreover, at diametrically opposite current elements, the 180-degree electrical phase shift plus the reversal of the direction of the current in space yield two radiating elements which are in phase and separated by a distance  $d_0$ . This condition, favorable for efficient radiation, will hold over diameters somewhat smaller and larger than  $d_0$ , so it is seen that the band around  $d_0$  is the important source for the radiated fields. Since the electrical phase change is 90 degrees per quarter turn along the spiral at diameter  $d_0$ , the resultant radiation is circularly polarized.

The radiation mode which occurs at the smallest diameter  $d_0 = \lambda/\pi$  is most frequently used, and requires out-of-phase currents at the spiral input terminals. The radiation pattern for this mode is a broad beam symmetrical about the axis of the spiral. For in-phase current excitation, the pattern is characterized by a split beam with an on-axis null.

4.1.3.2. Impedance and Matching. The input impedance to the spiral can be controlled by changing the ratio of arm spacing,  $b$ , to arm width,  $w$ . The most commonly used spirals are designed such that the arm width and the arm spacing are equal, i.e.,  $b/w = 1$ . For this self-complementary antenna the impedance is 180 ohms. This impedance can be decreased by making  $b/w$  larger. Conversely, this impedance can be increased by using a smaller ratio.

The spiral feed requires the use of a network with two outputs having a balanced capacitance to ground. In addition, the output currents must be out of phase to obtain the lowest mode of radiation from the two-arm spiral. This can be achieved simply by means of the balun shown in Figure 6. The two outputs for the balun are created by the tee. Arm A is adjusted to provide 180 degrees greater phase shift than Arm B at a given frequency so that the required out-of-phase currents are generated. This balun also provides a 1:4 impedance transformation between input and output. The major inherent limitation of the balun described is the narrow-band characteristics, but this is not a serious disadvantage for the measurements intended, since the balun can be retuned at each frequency to provide a proper match.

Another type of balun was considered which could be used to cover a frequency range of one octave with the spiral operating in the basic mode. The balun would utilize two broadband 90-degree phase shifters similar to those described by Schiffman (Reference 8). An operational balun of this type was reported by Craven (Reference 9). It would be convenient to construct this type of balun from simple stripline circuit elements. However, due to the high ratio ( $\rho$ ) of even-mode to odd-mode impedance needed for Schiffman's original design, realizing these phase shifters in dielectric-loaded stripline would be extremely difficult. For example, the clearance slit between two quarter-wavelength coupled sections would be only 0.002" for 1/4-inch ground

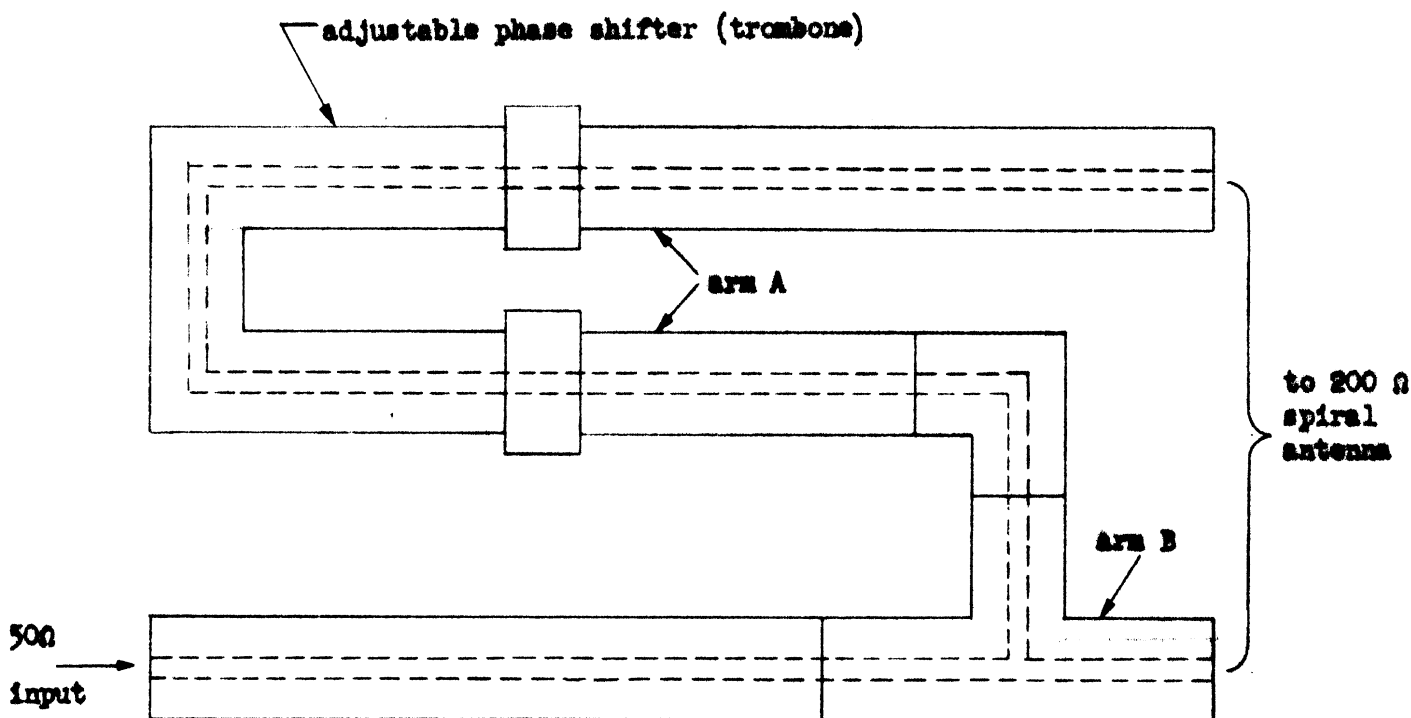


Figure 6. Coaxial Balun for Out-of-Phase Excitation

plane separation. For this reason a new design was developed for the phase shifters using much lower values of  $\rho$ . This change, however, yields faster phase deviation from 90 degrees, as a function of frequency, than does the original design. In order to counteract this frequency sensitivity, a more complicated network, called Type B by Schiffman, is necessary. The Type B phase-shift network consists of two sections of stripline having different values of  $\rho$ . Each section is one-quarter wavelength at the center frequency. With optimum values of  $\rho_1$  and  $\rho_2$  for this type of a network, a  $\pm 4.6$ -degree phase-shift deviation from 180 degrees results over a 2:1 bandwidth for the balun.

Since the construction and testing of the stripline balun would require considerable time, it was decided that the coaxial balun would be used for at least the initial spiral antenna measurements.



4.1.3.3. Construction of the Spiral. An Archimedean two-arm spiral, each arm consisting of eight full turns, was photoetched on a thin fiberglass base. The spacing between the arms was made equal to the conductor width of 0.049 inch. The spiral is located at the mouth of a cylindrical metal cavity approximately three and one-half inches in diameter and two inches deep (see Figure 7). The largest diameter to which the spiral arms extend is 3.35 inches. Therefore, there is a clearance of 0.1 inch between the outermost arm of the spiral and the inside diameter of the cavity. As shown in Figure 7, a two-wire open line connects the spiral to the input terminals on the back of the cavity. The characteristic impedance of this transmission line is tapered from 200 ohms at the input terminals to 180 ohms at the spiral to provide a matched feed from the coaxial balun. The cavity depth is one-quarter wavelength at 1.5 kilomegacycles per second. This frequency will be close to the low-frequency limit of the spiral, the diameter of the radiation band for this frequency occurring at 2.52 inches. If radiation from the outermost diameter for one arm, 3.19 inches, would still give a useable pattern, the lowest operating frequency would be fixed at 1.2 kmcs. The high-frequency limit will be determined by the cavity depth, due to the gain reduction occurring as a result of the reflections from the cavity back. According to experimental evidence the gain will be reduced by 3 db when the cavity depth becomes equal to three-eighths wavelength, resulting a high-frequency limit of 2.25 kmcs. for the present spiral-cavity combination. Another possible high-frequency limitation would be the appearance of the first split-beam mode at 2.36 kmcs. The proper operating range for the spiral and balun combination will be determined by taking pattern measurements, which will indicate the low-frequency and high-frequency limits of the spiral by a deterioration of the regular pattern.

ID = 0.563 in.  
 OD = 0.625 in.  
 d = 0.244 in.  
 s = 0.669 in.

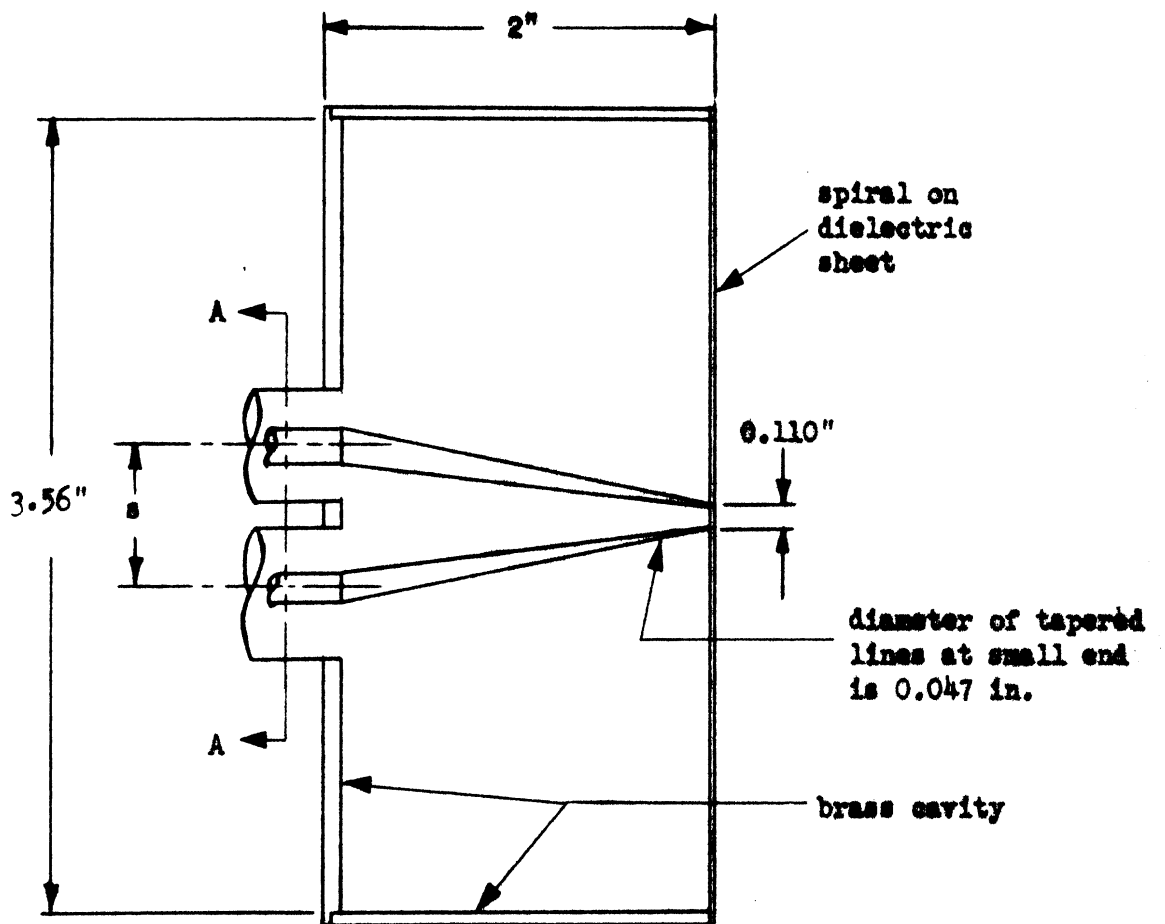
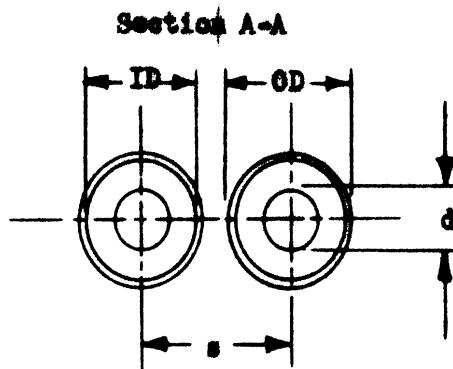


Figure 7. Cavity and Spiral Feed

## 4.2. EXPERIMENTAL STUDIES

X-band slot coupling measurements, similar to those reported last period, were made to determine (1) the effects upon the magnitude of slot-to-slot coupling introduced by locating one of the slots near an edge of the ground plane, (2) the effects upon the magnitude of coupling due to slots oriented at various angles to each other, and (3) a method for measuring the phase of coupling between slots.

S-band measurements were made to develop a waveguide-to-monopole transformer which matches the monopole impedance to the impedance of a waveguide through a tapered ridge and an adjustable short network.

4.2.1. SLOT COUPLING MEASUREMENTS. More slots were added to the ground plane (used for previous coupling measurements) for the purpose of measuring and evaluating edge effects upon the two-slot coupling magnitude. A second ground plane was constructed with a rotatable slot so that the magnitude of coupling between two slots oriented at various relative angles could be measured. Phase measurements of the coupling associated with these magnitude measurements were attempted. However, the accuracy and repeatability of these measurements were very poor. Improvement in the phase measurements was obtained by making various modifications to the microwave bridge arrangement used for the coupling measurements. These modifications consisted of replacing some of the microwave components with less phase-sensitive components, rearrangement of the bridge so that equal length arms existed in the bridge, and the utilization of a slotted line for measuring the phase instead of a phase shifter.

4.2.1.1. Edge Effects. Two more slots have been added to the 24" x 36" brass ground plane, as shown in Figure 8, to experimentally determine the magnitude of edge effects upon measured slot coupling. One of the new slots (No. 8) is spaced 7.67 wavelengths from slot No. 6 and 6.80 wavelengths from the nearest edge of the ground plane. The second new slot (No. 9) is spaced 7.67 wavelengths from slot No. 3 and 0.727 wavelength from the nearest edge of the ground plane. Measured coupling between slot No. 6 and slot No. 8 is -38.6 db at 9.20 kmcs; measured coupling between slot No. 3 and slot No. 9 is -38.4 db. The small difference between these two measured values suggests that edge effects are negligible. Before concluding thus, the distance between one slot and the edge of the ground plane, as well as the slot attitude relative to the edge, should be varied and measurements repeated for these general cases.

4.2.1.2. Absorbent Shield. The equipment used for the experimental measurement of X-band slot coupling factor is extremely sensitive to microwave scatterers in the vicinity of the ground plane containing the slots. For example, personnel within ten or fifteen feet of the slots can cause intolerable variations in the null detector signal. To overcome this problem, a miniature microwave anechoic chamber (see Figure 9) was constructed to enclose the ground plane and slots, thus providing a shield from external objects and personnel.

The shield was constructed from plywood and four-inch "Hairflex" microwave absorber manufactured by B. F. Goodrich. Twine was used to "sew" the edges of the plywood together so that reflections would be minimized.

With the microwave absorber shield in place, the null detector signal was sufficiently quiet to facilitate repeatable and accurate slot coupling

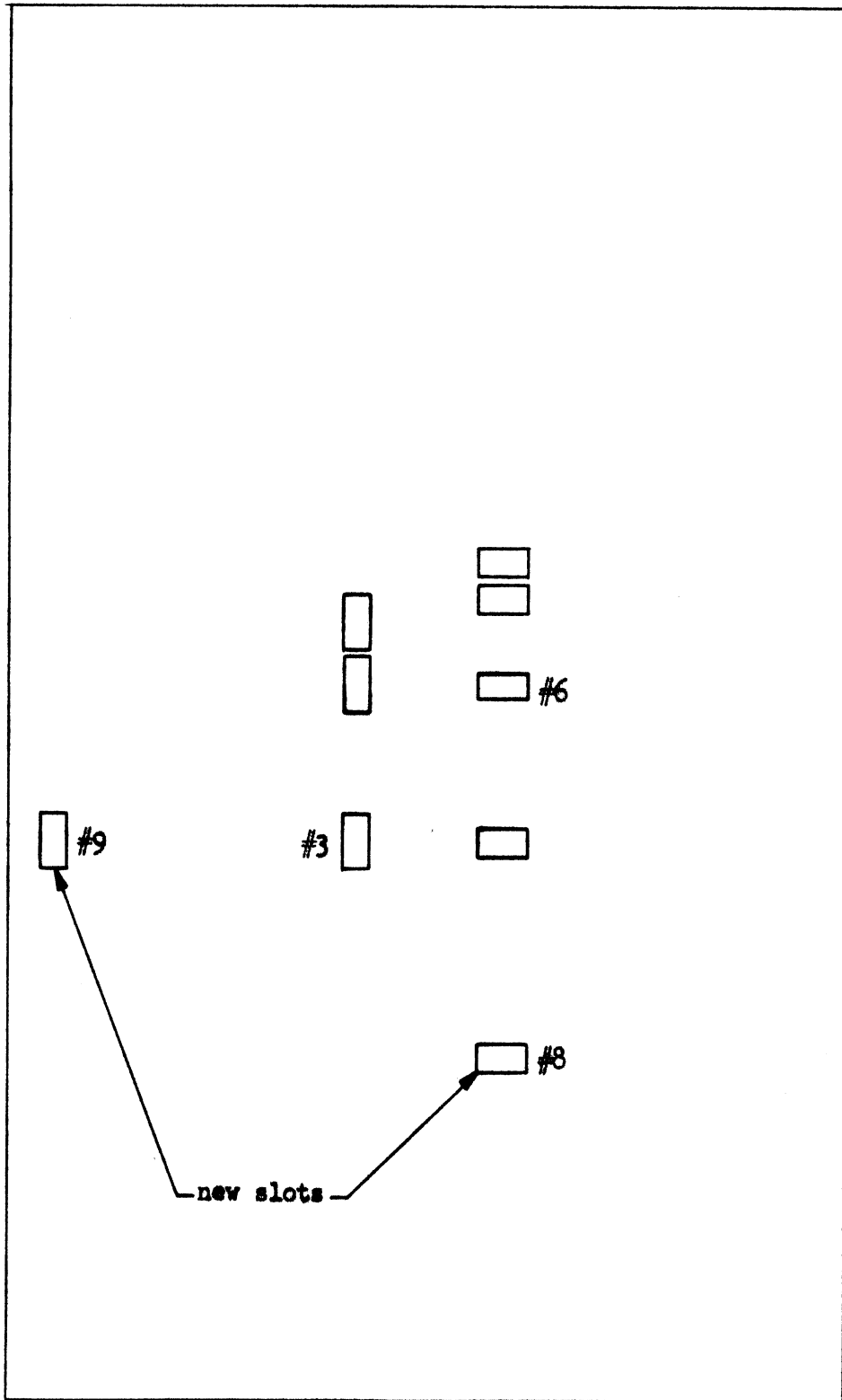


Figure 8. Ground Planes Used for Edge Effect Measurements

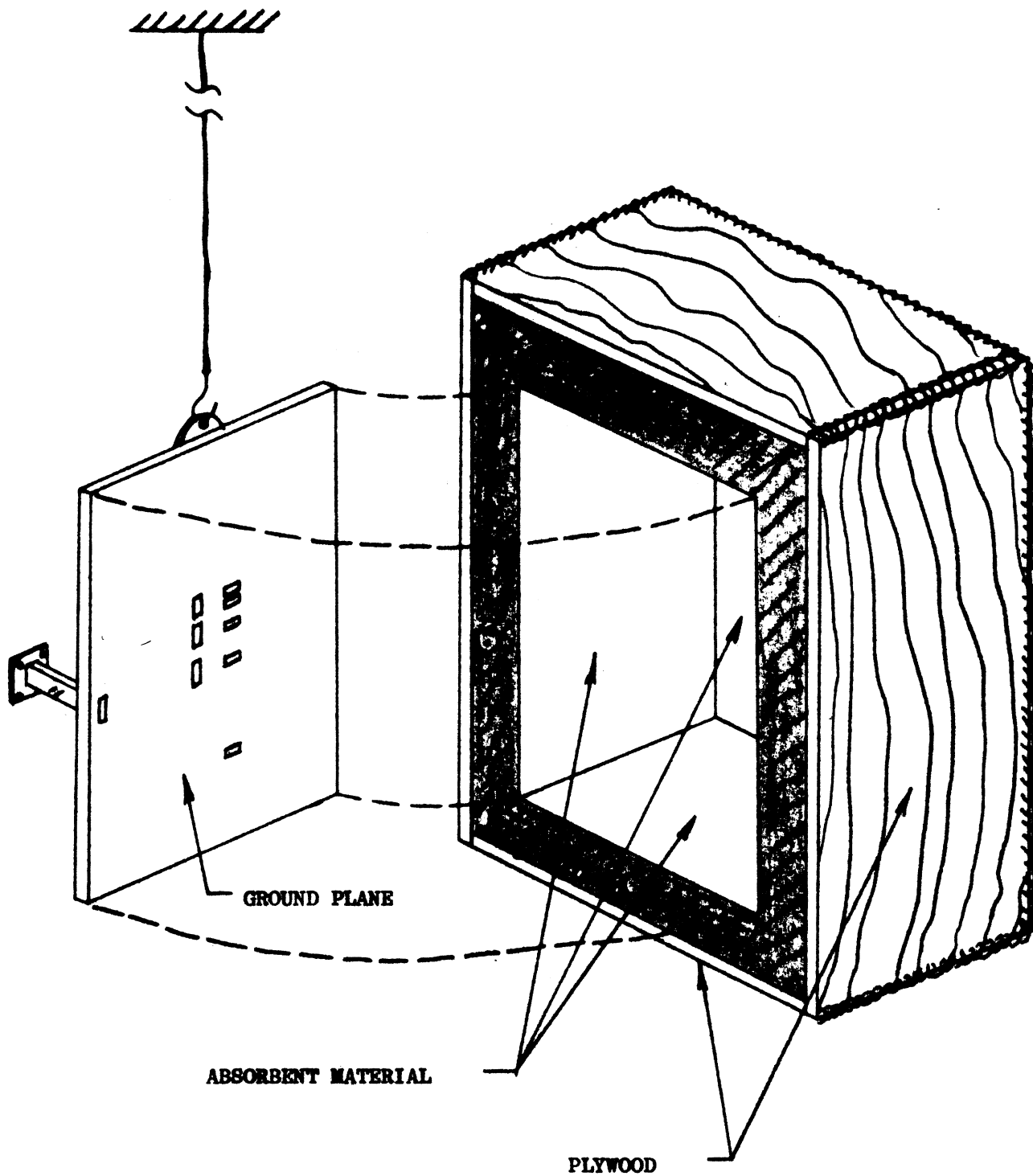


FIGURE 9. ABSORBENT SHIELD

measurements. The effect of the shield upon the waveguide-to-slot impedance match is barely detectable, even for the slot near one edge of the ground plane (slot No. 9 in Figure 8). The effect of the shield upon measured slot-to-slot coupling is also negligible.

4.2.1.3. Coupling Between Two Slots of Arbitrary Orientation. Let two slots, spaced  $\frac{d}{\lambda}$  wavelengths apart, be oriented at arbitrary angles, defined as  $\alpha$  and  $\beta$ , as shown in Figure 10. The magnitude of the coupling factor is a function of  $\frac{d}{\lambda}$ ,  $\alpha$ , and  $\beta$ . To obtain a crude but quick experimental check for the theoretical predictions of this coupling factor, measurements of coupling were made using slot No. 1, No. 2, or No. 3 with slot No. 4, No. 5, No. 6, or No. 7 (see Figure 11). With these seven slots, ten distinct combinations of  $\frac{d}{\lambda}$ ,  $\alpha$ , and  $\beta$  were possible, limited in variety because (a) one slot orientation was always ninety degrees from the second slot orientation, and (b) the vertical component of the separation between the two slots was always equal to two wavelengths at the operating frequency.

The results for the ten possible cases (refer to Figure 11) are given in Table I. The slot separation,  $\frac{d}{\lambda}$ , and the angles  $\alpha$  and  $\beta$ , were calculated from measured values of the variable horizontal component of the separation,  $\frac{D}{\lambda}$ . Coupling (K) is given in decibels referred to unity coupling (0 db).

4.2.1.4. New Ground Plane With Rotatable Slot. In order to obtain a more flexible means for comparing experimental values of slot-to-slot coupling with those predicted by theory, a new copper ground plane with four fixed slots and one rotatable slot was constructed, and is shown in Figure 12. The mechanical detail of the rotatable slot is shown in Figure 13. A dial on the back of the ground plane indicates the orientation angle of the rotatable slot, relative to an adjustable reference angle.

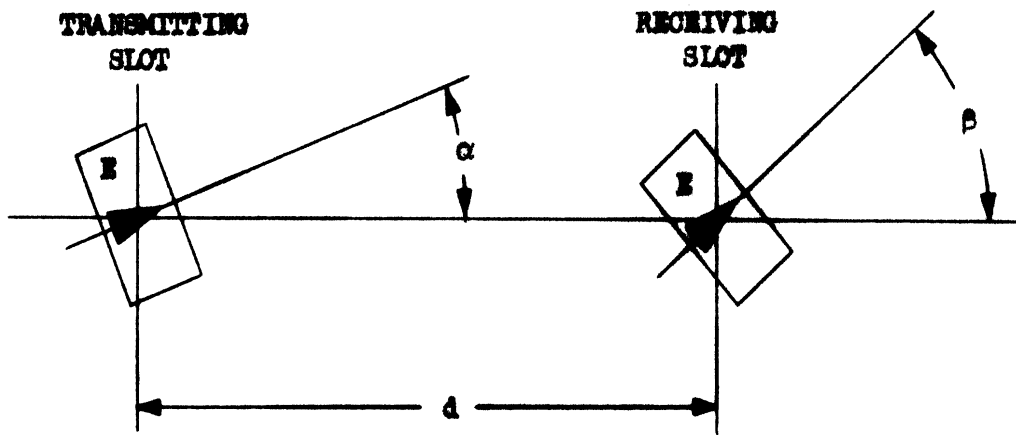


Figure 10. Two Arbitrarily Oriented Slots

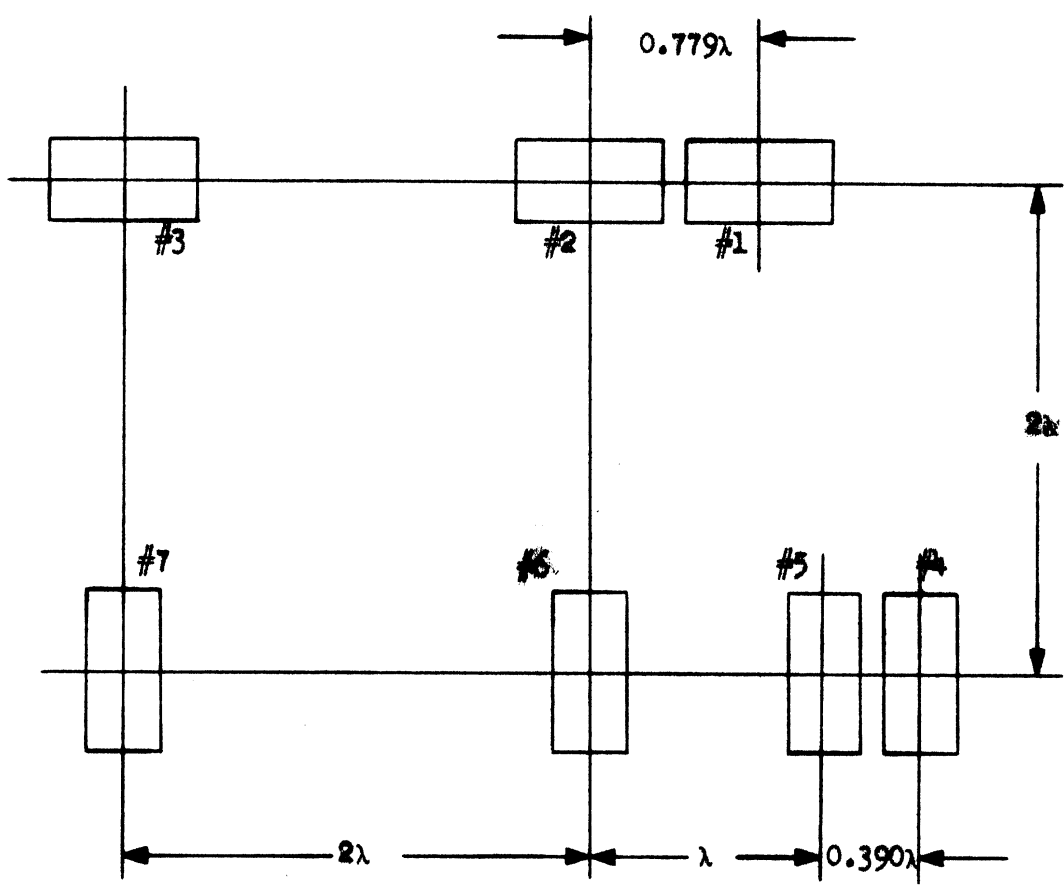


Figure 11. Slot Layout for Preliminary Coupling Measurements



TABLE I

Slots Used		$\frac{D}{\lambda}$	$\frac{d}{\lambda}$	$\alpha$	$\beta$	K
XMTR	RCVR					
No. 7	No. 3	0.000	2.000	+90.0°	0.0°	-72 db (approx.)
No. 5	No. 1	0.221	2.015	+83.7°	- 6.3°	-46.6 db
No. 1	No. 4	0.611	2.092	+163.0°	+73.0°	-39.4 db
No. 6	No. 1	0.779	2.146	+111.3°	+21.3°	-38.3 db
No. 5	No. 2	1.000	2.236	+ 63.4°	-26.6°	-37.2 db
No. 2	No. 4	1.390	2.436	- 34.8°	+55.2°	-36.0 db
No. 6	No. 3	2.000	2.828	+ 45.0°	-45.0°	-37.1 db
No. 1	No. 7	2.779	3.424	-125.7°	-35.7°	-38.8 db
No. 7	No. 1	2.779	3.424	+144.3°	+54.3°	-38.9 db
No. 5	No. 3	3.000	3.606	+ 33.7°	-56.3°	-39.8 db
No. 3	No. 4	3.390	3.936	- 59.5°	+30.5°	-41.4 db

f = 9.20 kms

$\lambda = 1.283$  inch

These data have been plotted in Figure 5.

The coupling between fixed slots B and C and the rotatable slot, A, were measured for  $\alpha = 0$ ,  $-\frac{\pi}{2} \leq \beta \leq \frac{\pi}{2}$ , in five-degree increments (refer to Figure 10). Measured coupling data, in decibels below unity coupling, have been shown in the curves of Figure 4. It was observed that the phase of the coupling, with respect to the variable,  $\beta$ , was essentially constant. Truly dependable

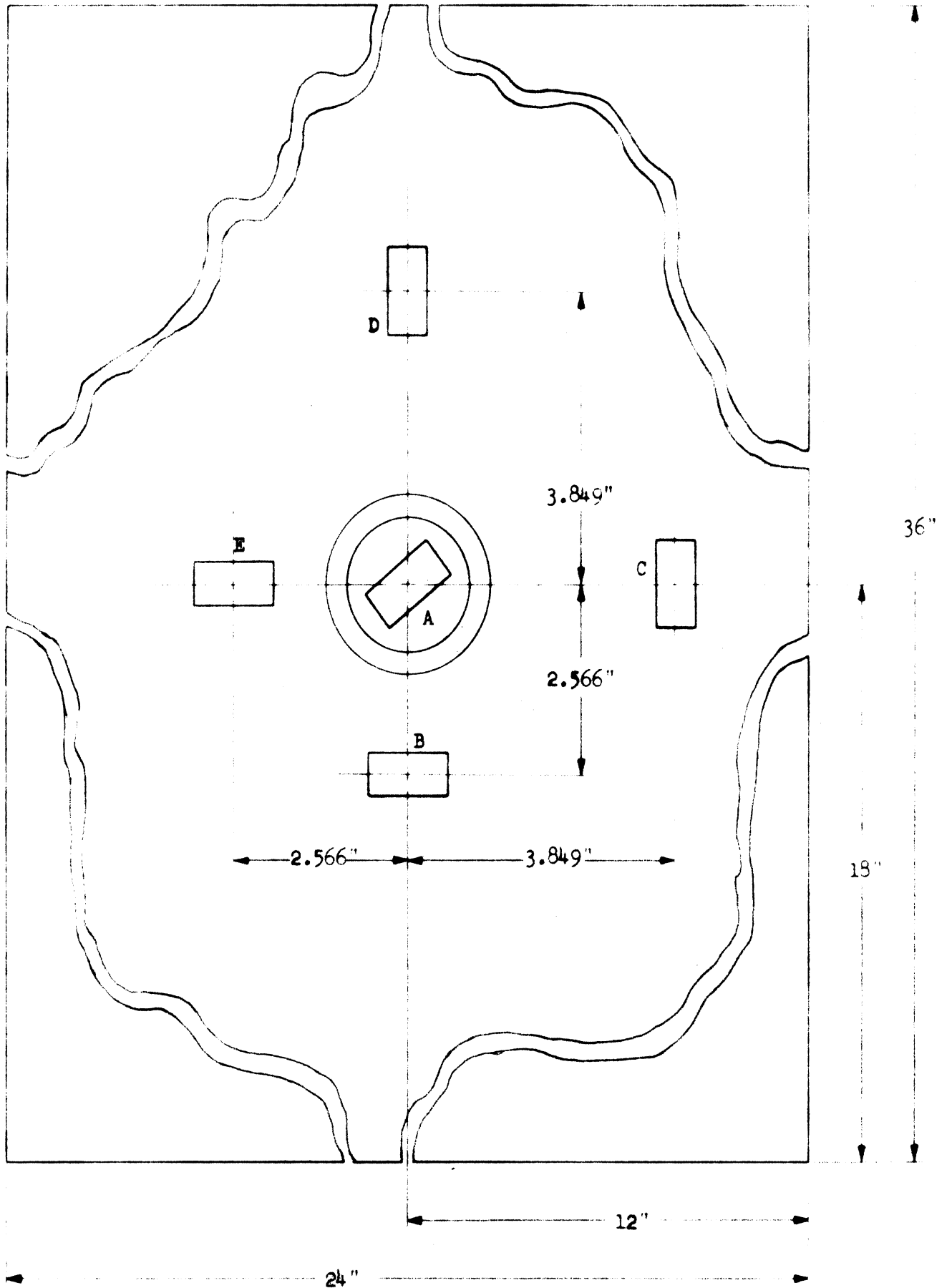


Figure 12. New Ground Plane with Rotatable Slot

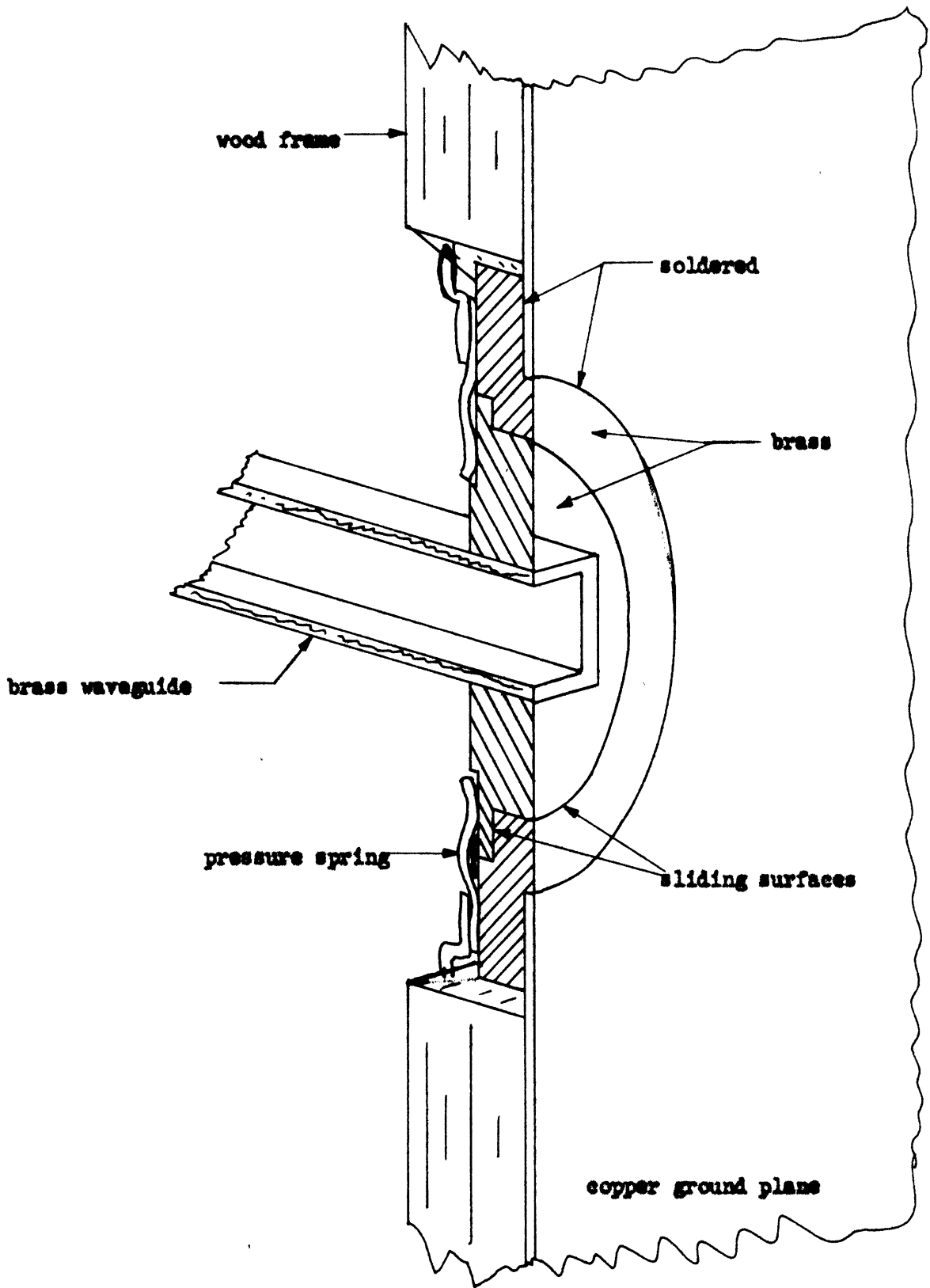


Figure 13. Mechanical Detail of Rotatable Slot

phase measurements were impossible because of the poor phase stability ( $\pm 15^\circ$ ) of the coaxial cables which couple the slots to the microwave bridge.

An effort was made to measure secondary coupling, which consists of coupling between two slots via a third slot (terminated with a matched load) with the two primary slots decoupled ( $\alpha = 0^\circ$ ,  $|\beta| = 90^\circ$ ). Two such configurations were used: (1) slots A and B as primaries, slot C as the intermediate, and (2) slots A and C as primaries, slot B as the intermediate. Coupling should be approximately -70 db for these configurations. This coupling factor was not measurable because of reflections caused by the connecting cables and adaptors.

4.2.1.5. Improved Connecting Cables. New coaxial cables with double-stub tuners were used in an effort to obtain the phase and low-level coupling measurements discussed above. The phase stability was improved somewhat ( $\pm 10^\circ$ ), but the matching stubs could not be set so that reflections would be minimized for many cable positions. Obviously, some other means of coupling the slots to the microwave bridge was necessary in order to obtain sufficiently accurate coupling data.

4.2.1.6. Rotary Joint Connecting Arms. Two forms of rotary joints, in conjunction with waveguide bends and straight sections, were considered as means for improving measurement accuracy. The first form consisted of two waveguide-to-coax adaptors joined by a dual female N-type connector. Five of these joints were required to couple one fixed slot and one rotatable slot to the microwave bridge. In order to move the rotatable slot, or to change from one fixed slot to another, it was necessary to loosen the connector at each joint, move the "flexible" arms to the new position, and retighten each connector.

Although this method of coupling resulted in smaller reflections ( $V_{SWR} < 1.05$ ), the phase stability (or repeatability) was still not better than  $\pm 3^\circ$ .

Five precision waveguide rotary joints were next considered. Operating at a frequency of 9.2 kmcs. (that used for previous measurements), a phase stability better than  $\pm 1^\circ$  was observed while moving these joints to all possible positions.

4.2.1.7. Characteristics of Waveguide Rotary Joints. Because these rotary joints are relatively narrow-band devices, it was thought best to determine the optimum frequency of operation. Figure 14 shows the VSWR obtained for each rotary joint as a function of frequency. In order to minimize reflections, a frequency of 9.29 kmcs. was selected as optimum. Rotary joints No. 5, No. 2, and No. 4, because of their similar characteristics, were selected to couple the rotating slot to one terminal of the microwave bridge (see Figure 15). Likewise, rotary joints No. 3 and No. 1 were selected to couple the fixed slot to the other bridge terminal. The phase and magnitude of the worst reflection, which is a function of the angular position of the rotary joints, were determined for each connecting arm. In order to minimize these reflections, a double-stub waveguide tuner was designed and constructed for each set of rotary joints.

At this point, phase stability was rechecked and found to be better than  $\pm 1/2^\circ$ . Since this stability is entirely adequate for the intended coupling measurements, all waveguide slots were retuned for a perfectly matched input at 9.29 kmcs.

4.2.1.8. Performance of Microwave Bridge Employing Rotary Joints. The microwave bridge (shown in Figure 7 of Interim Technical Report No. 1) was tested with a typical configuration of two-slot coupling, using the five waveguide rotary joints to connect the slot waveguides to the bridge terminals.

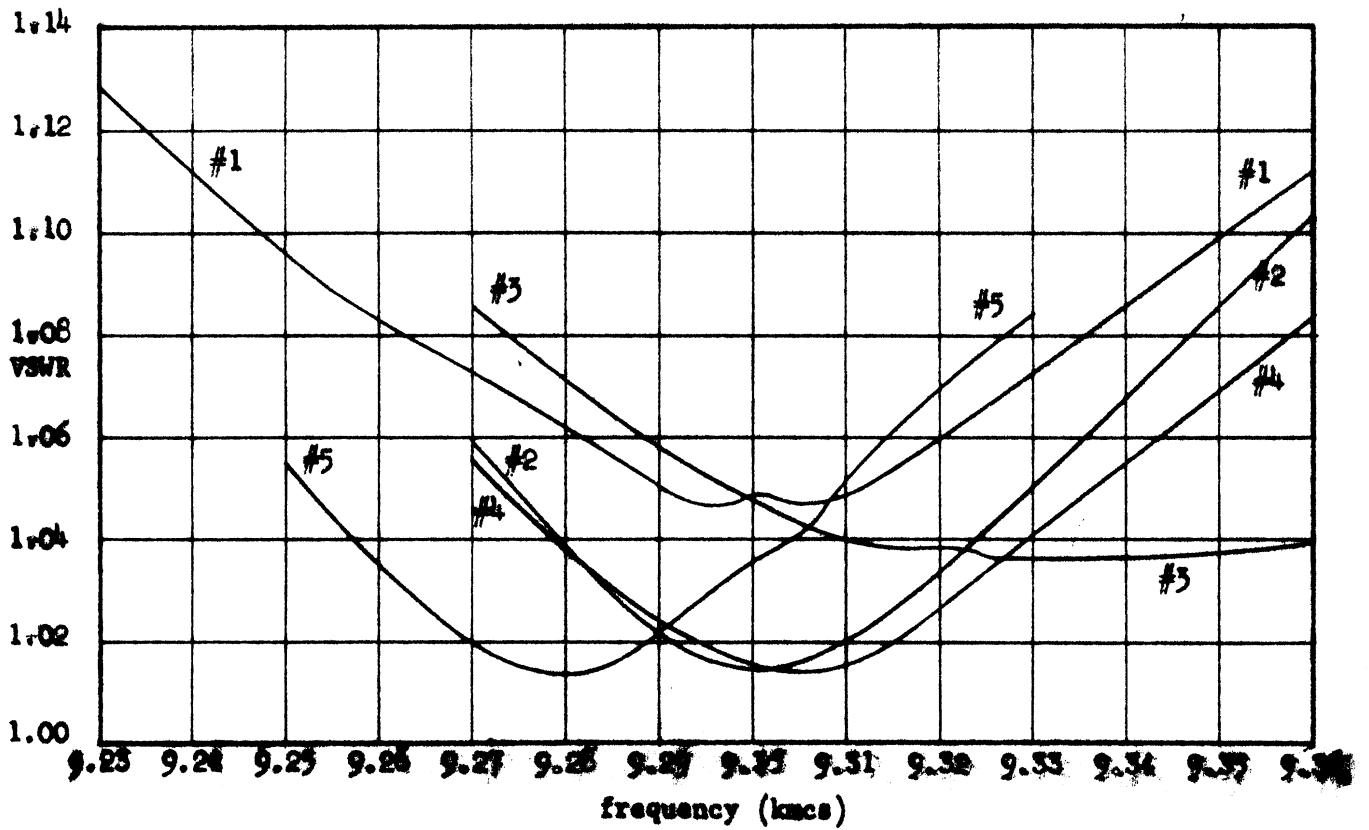


Figure 14. VSWR of Rotary Joints versus Frequency

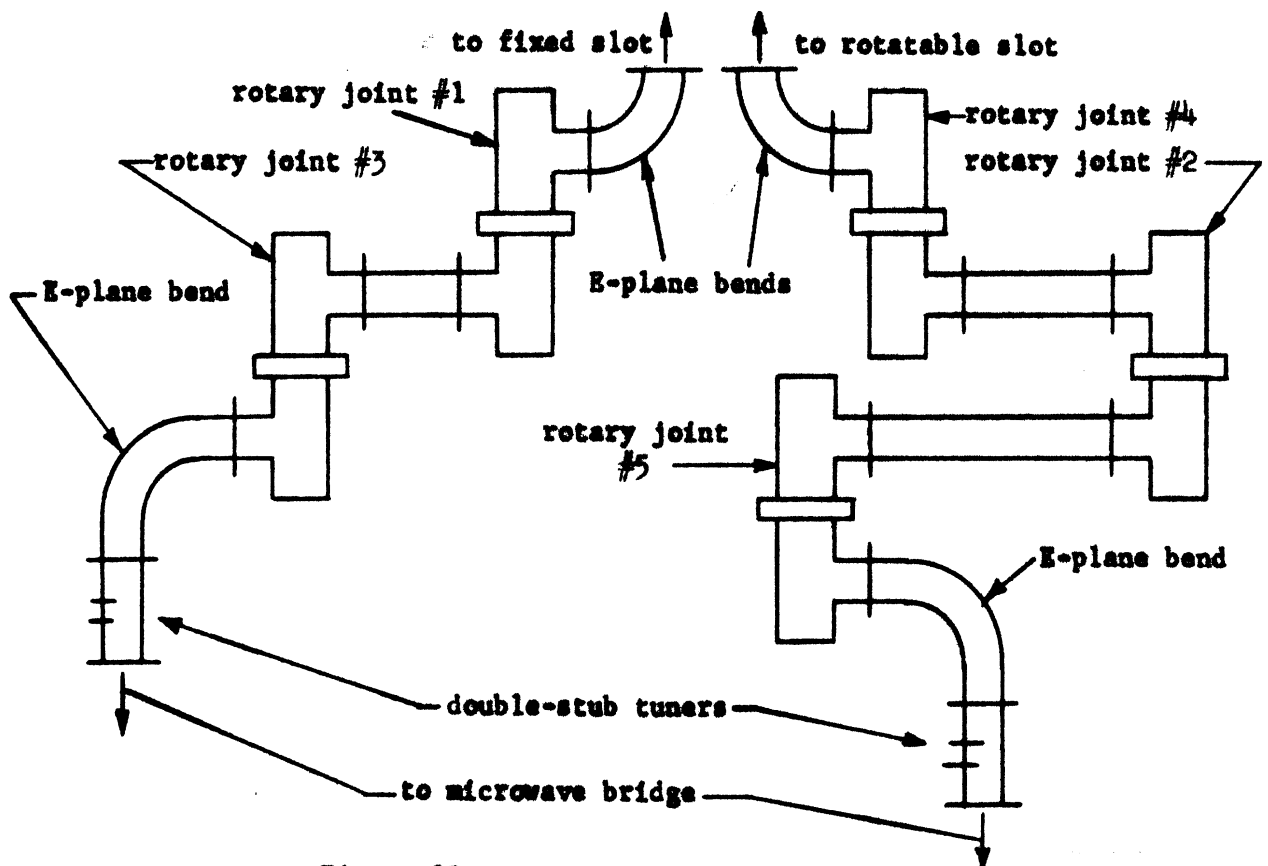
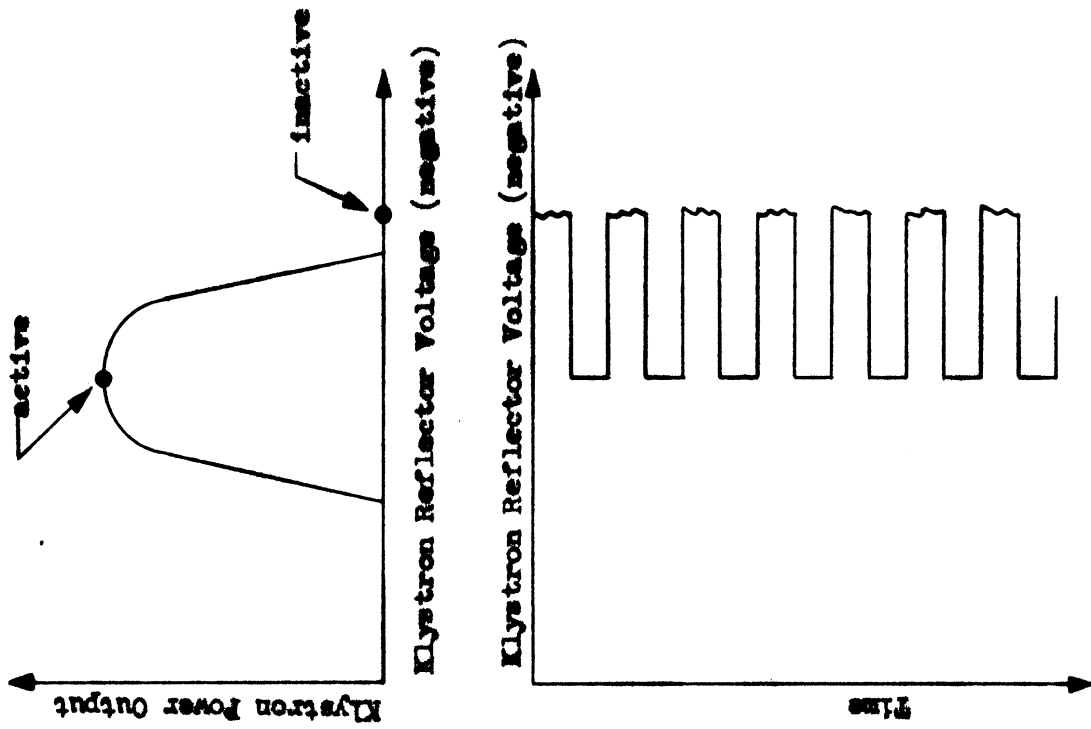


Figure 15. Rotary Joint Connecting Arms

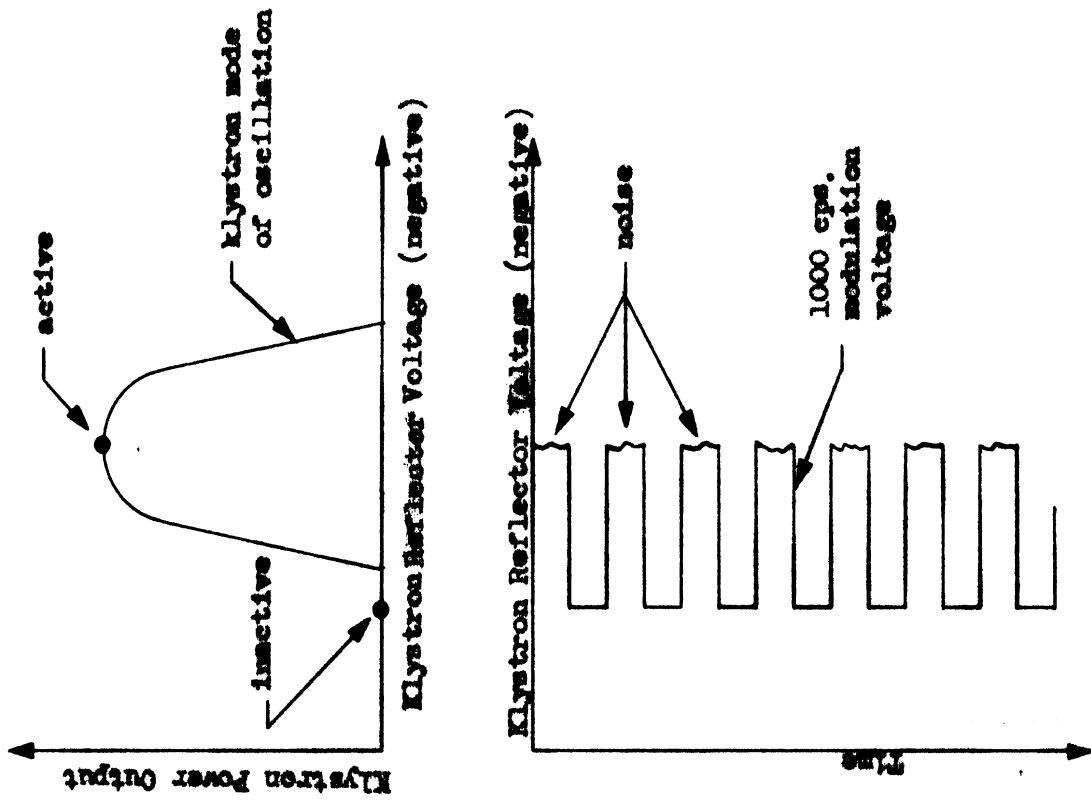
The best null obtainable, however, was only 20 db below the bridge input power level, which resulted in a rather broad null and poor repeatability. This phenomenon was explained by the presence of incidental frequency modulation of the klystron oscillator; since each bridge arm represents an electrical length of several wavelengths, the microwave signal undergoes considerable phase shift in propagating through each arm. This phase shift is directly related to the frequency for small frequency deviations, and increases with increasing electrical length of the bridge arm. Hence, a frequency-modulated signal applied to the input of each bridge arm results in a frequency- and phase-modulated signal at the output. If the two bridge arms are not of equal electrical lengths, then the difference in the phase modulation of the two microwave signals appears at the null detector. Since a perfect null can only be produced at the instant when the relative phase of the two signals is  $180^{\circ}$ , an amplitude modulation of the null signal results from the modulation of the relative phase of the two signals from the bridge arms. The null meter will thus respond to the average null signal which is considerably higher than the best instantaneous null signal, hence a broad null of large amplitude results.

The incidental frequency modulation was partially attributable to ripple and/or noise present on the active side of the square-wave modulation signal (see Figure 16a) in the klystron power supply. By raising the reflector voltage, the square wave was shifted as shown in Figure 16b. This placed the opposite side of the square wave in the active position on the klystron mode, and resulted in less frequency modulation.

To reduce the sensitivity of the microwave bridge to frequency modulation and thereby improving the null still further, it was necessary to equalize the electrical lengths of each bridge arm. To facilitate this change, and to



(a) Method which results in considerable frequency modulation.



(b) Method employed to reduce frequency modulation.

Figure 16. Methods of Klystron Amplitude Modulation



minimize insertion loss in the bridge arms (so as to maximize the null-signal to meter-noise level), the two 10-db directional couplers were replaced with waveguide tees. The resultant layout of the modified microwave bridge is shown in Figure 17. Note that the precision phase shifter has been moved from the "unknown" arm to the reference arm to help equalize their lengths. An additional attenuator was required in the "unknown" arm to offset the insertion loss of the phase shifter so that the bridge could be balanced, with no slots connected, for reference phase and attenuation.

The accuracy of this bridge was tested by inserting various lengths of waveguide between the "unknown" terminals, where the slot waveguides would normally be connected. The attenuation of these waveguide sections is negligible; the phase shift of each was calculated from measurements of their physical dimensions. Table II shows the measured attenuation and phase shift versus the calculated phase shift for these sections.

TABLE II

Calculated Phase Shift	Measured Phase Shift	Error	Measured Attenuation
0.0° (reference)	0.0°	0.0°	0.00 db
11.9°	12.9°	+1.0°	-0.13 db
53.0°	58.5°	+5.5°	-0.41 db
238.9°	240.3°	+1.4°	+0.07 db
292.0°	294.0°	+2.0°	+0.17 db

4.2.1.9. Replacement of Output Tee and Phase Shifter with Slotted Line.

The errors indicated in Table II are at least partially attributable to interaction of the reflections from the phase shifter and reflections from other

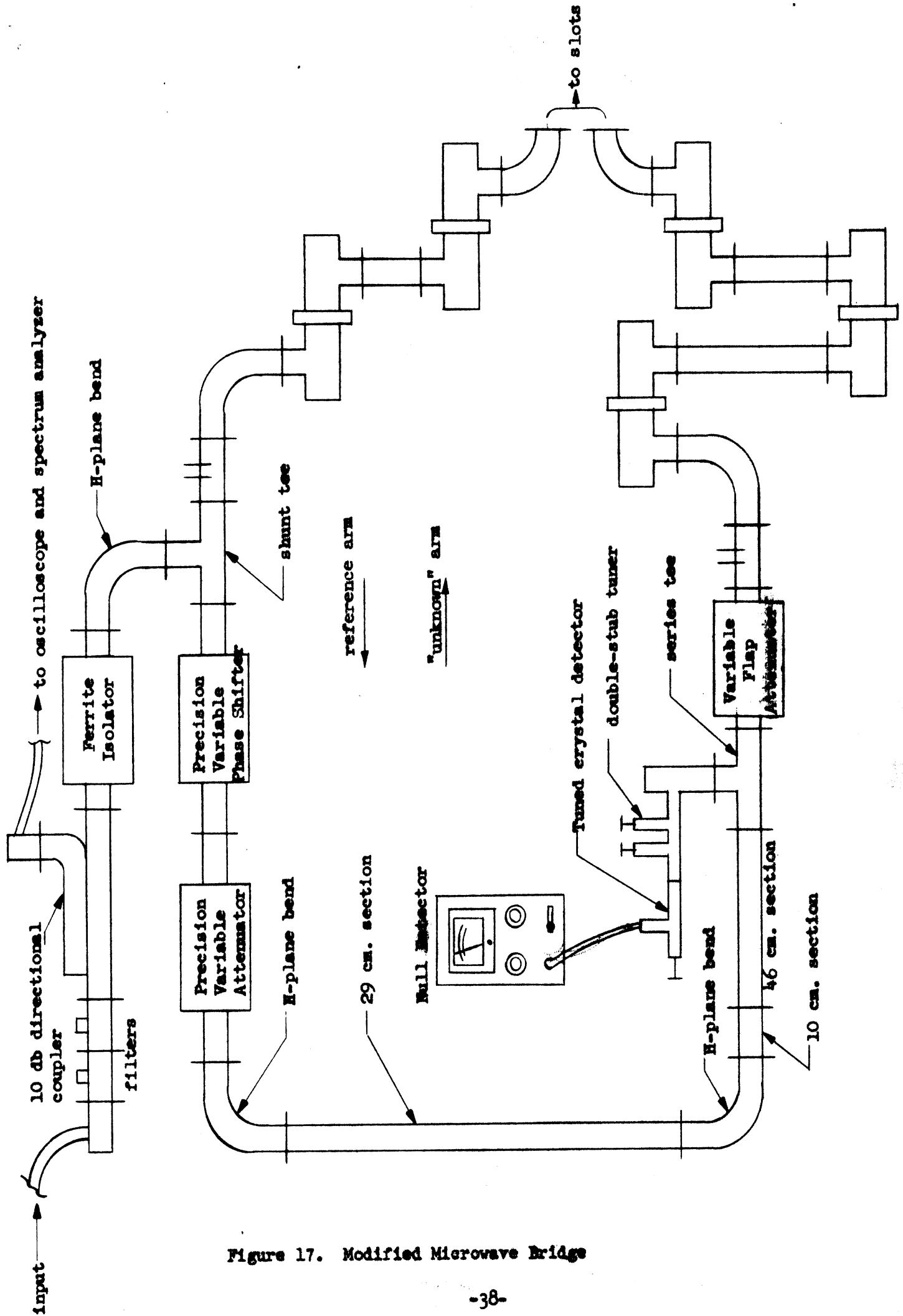


Figure 17. Modified Microwave Bridge

components of the microwave bridge, hence another revision to the bridge was made: The precision variable phase shifter was removed from the reference arm and the output tee was replaced with a slotted section for phase measurements. These two changes gave rise to a two-fold improvement: (1) reflections from the phase shifter were eliminated, and (2) the relative phase relationship among other reflections was held fixed.

The further revised bridge was tested in two ways: First, the "tracking" of the precision variable attenuator in the reference arm with respect to the variable flap attenuator in the "unknown" arm was obtained by setting the variable flap attenuator to a given value and recording the setting of the precision variable attenuator required to rebalance the bridge. These data are listed in Table III. The gradual deviation of one attenuator from

TABLE III

<u>Variable Flap Attenuator Setting (db)</u>	<u>Precision Variable Attenuator Setting (db)</u>
0	0.04
1	1.17
2	2.23
3	3.30
4	4.31
5	5.40
6	6.31
7	7.51
8	8.52
9	9.66
10	10.74
12	12.66
14	14.71
16	16.67
18	18.77
20	20.73
MAX.	26.95

the other is most likely due to calibration error of the variable flap attenuator, while the irregular deviations probably constitute actual measurement errors due to reflections within the microwave bridge. Second, the bridge was again tested

with several straight waveguide sections as "unknown" insertion networks.

Table IV shows the measured attenuation and phase shift versus the calculated phase shift for each section. The calculated values of phase shift in the

TABLE IV

Calculated Phase Shift	Measured Phase Shift	Error	Measured Attenuation
0.0° (reference)	0.0°	0.0°	0.00 db
13.2°	13.0°	-0.2°	-0.02 db
52.7°	50.7°	-2.0°	-0.04 db
235.1°	233.6°	-1.5°	+1.22 db
402.8°	408.9°	+6.1°	-0.05 db
637.9°	638.2°	+0.3°	+0.14 db
769.3°	767.2°	-2.1°	-0.03 db
1196.2°	1192.5°	-3.7°	-0.11 db
1407.2°	1409.7°	+2.5°	+0.07 db
1965.5°	1965.9°	+0.4°	+0.01 db
2018.2°	2023.7°	+5.5°	+1.50 db
3617.5°	3616.5°	-1.0°	+0.06 db

table above were obtained thus: Consider the phase shift of a given waveguide section as having two components, and expressable as

$$\phi = n\pi + \theta \text{ radians,} \quad (31)$$

where n represents the number of multiple half-wavelengths included in the total length of the section. The value of n was determined from an approximate measurement of the physical length of the waveguide section and a knowledge of the guide wavelength. The remaining phase shift,  $\theta$ , was determined from a precise slotted line measurement. The slotted line was first terminated with a shorting

plate, and the positions of the voltage minima noted. Then the unknown waveguide section was inserted between the slotted line and the shorting plate, and the new positions of the voltage minima noted. The value of  $\theta$  was then calculated from the direction and magnitude of the shift of the voltage minima using the equation

$$\theta = \frac{2\pi s}{\lambda_g} \text{ radians,} \quad (32)$$

where  $s$  = shift of the voltage minima toward the load,

$\lambda_g$  = guide wavelength at the operating frequency.

Errors presented in the data of Table IV indicate the presence of serious residual reflections within the microwave bridge. The only bridge component still remaining which could have caused these reflections was the input shunt tee. To reduce this problem, a hybrid tee was substituted for the shunt tee. The fourth port (series arm) was terminated with a matched load to help absorb unwanted reflections. The measurements taken with the shunt tee were repeated and are shown in Table V. Some improvement is indicated, but errors are still excessive.

TABLE V

Calculated Phase Shift	Measured Phase Shift	Error	Measured Attenuation
0.0°(reference)	0.0°	0.0°	0.00 db
235.1°	237.5°	+2.4°	+0.44 db
637.9°	639.9°	+2.0°	+0.41 db
1196.2°	1191.7°	-4.5°	-0.13 db
1965.5°	1962.0°	-3.5°	-0.04 db
2018.2°	2018.6°	+0.4°	+0.30 db

4.2.1.10. Final Consideration of Bridge Inaccuracies. In order to maximize the accuracy of the microwave bridge, the following steps were considered:

- a. Measure and minimize all possible reflections.
- b. Precisely equalize bridge arms, using a typical slot-to-slot separation, so that the null signal is most free from noise and effects of residual frequency modulation.
- c. Use ferrite isolators and/or padder attenuators in both bridge arms to minimize interaction.
- d. Replace hybrid tee with matched hybrid tee to minimize interaction.
- e. Use less probe penetration in slotted line detector.

All components used in the microwave bridges described were tested for quality of performance at the selected frequency of 9290 megacycles per second. The rotary joints were tested in the exact form used for the microwave bridge, as described in Section 4.2.1.7 and shown in Figure 15, i.e., as connecting arms for the slots. Results of these measurements, taken while moving the rotary joints to all possible orientations, are:

Connecting arm for rotary slot

Maximum VSWR = 1.043

Minimum VSWR = 1.022

Connecting arm for fixed slot

Maximum VSWR = 1.033

Minimum VSWR = 1.021

Two ferrite isolators were also tested for further consideration of point (c) above. The data for these two components are:

Ferrite Isolator (Litton X-250)

Input VSWR = 1.010                      Insertion Loss = 0.4 db

Output VSWR = 1.014                     Isolation = 14.5 db

Ferrite Isolator (Uniline H-86-96)

Input VSWR = 1.051                     Insertion Loss = 0.4 db

Output VSWR = 1.044                     Isolation = 10.3 db

Several other components were tested, yielding the following data:

Termination (Microline 150)

VSWR = 1.013

Termination (HP X910B)

VSWR = 1.025

} used for VSWR measurements

Precision Variable Phase Shifter (HP X885A)

Maximum VSWR = 1.105                  Minimum VSWR = 1.004

Precision Variable Attenuator (HP X382A)

Maximum VSWR = 1.041                  Minimum VSWR = 1.038

Variable Flap Attenuator (HP X375A)

Maximum VSWR = 1.034                  Minimum VSWR = 1.005

Shunt Tee (shop)

VSWR of shunt arm = 3.00

VSWR of symmetrical arms = 1.56

Series Tee (HP X840A)

VSWR of series arm = 2.40

VSWR of symmetrical arms = 1.56

Hybrid Tee (DeMornay-Budd)

VSWR of shunt arm = 3.00

VSWR of series arm = 1.95

VSWR of symmetrical arms = 1.17

Matched Hybrid Tee (Aircom 109-X-1 — matched at 9.0 kmc.)

VSWR of shunt arm = 1.12

VSWR of series arm = 1.54

VSWR of symmetrical arms = 1.17

In order to test the merit of point (d) above, the hybrid tee and the matched hybrid tee were tested for isolation between symmetrical arms: An adjustable short was connected to one symmetrical arm, the short arm and the series were terminated with matched loads, and the second symmetrical arm was regarded as the input. While adjusting the short through more than one-half wavelength, the input VSWR (ideally 1.000) was measured:

Hybrid Tee (DeMornay-Budd)

Maximum VSWR = 1.73

Minimum VSWR = 1.18

Matched Hybrid Tee (Aircom 109-X-1 — matched at 9.0 kmc.)

Maximum VSWR = 1.22

Minimum VSWR = 1.14

These data show that considerably better isolation can be obtained by using the matched hybrid tee. Hence, one final step in perfecting the microwave bridge will be to replace the hybrid tee with the matched unit. Data on the precision phase shifter confirm the wisdom of its replacement with the slotted line for phase measurements. The two attenuators incorporated thus far, based on the above data, should cause no problem. The rotary joint connecting arms should likewise cause little trouble. When the physical dimensions of the bridge arms were modified to accept the matched hybrid tee, the reference arm was carefully designed to balance the "unknown" arm thus satisfying point "b" above. Finally, it was concluded that less probe penetration would not affect the bridge accuracy (point "c" above) because at a null, the probe is at a point of near-zero impedance.



The final bridge design is shown in Figure 18, and incorporates all of the above considerations. Although no measurements have been made with this bridge at the time of this writing, slot coupling factors should be measurable within plus or minus one-half decibel in magnitude and within plus or minus three degrees in phase.

4.2.1.11. Measurement of Slot Coupling Phase. The phase of the two-slot coupling factor will be referred to the conducting ground plane and will include the two slot apertures proper. From Figure 19, it can be seen that this phase angle,  $\theta$ , cannot be directly measured due to the presence of the input waveguides and associated tuning screws. The phase angle  $\theta_m$  can be measured readily, and is directly related to the unknown  $\theta$  by the equation:

$$\theta_m = \theta + 2\phi + \phi_1 + \phi_2 \quad (33)$$

where  $\phi$  = phase shift introduced by each set of tuning screws

$\phi_1$  = phase shift due to length  $l_1$

$\phi_2$  = phase shift due to length  $l_2$

The greatest problem in the measurement of the coupling phase angle  $\theta$  is to determine the value of  $\phi$  so that  $\theta$  may be calculated from  $\theta_m$ . Since there is no analytical method available to calculate  $\phi$  with sufficient accuracy, a method for measuring this phase shift has been developed. Note that if the straightforward method of Section 4.2.1.9 were attempted, using a slotted line and a shorting plate, a serious error could result from the characteristic S-curve caused by the interaction of the reflections from the tuning screws and the shorting plate.

The method devised for this measurement employs two slot input waveguides of any length connected back-to-back through a short section (see Figure 20). Before connecting these slot waveguides thus, each is tuned for a match while

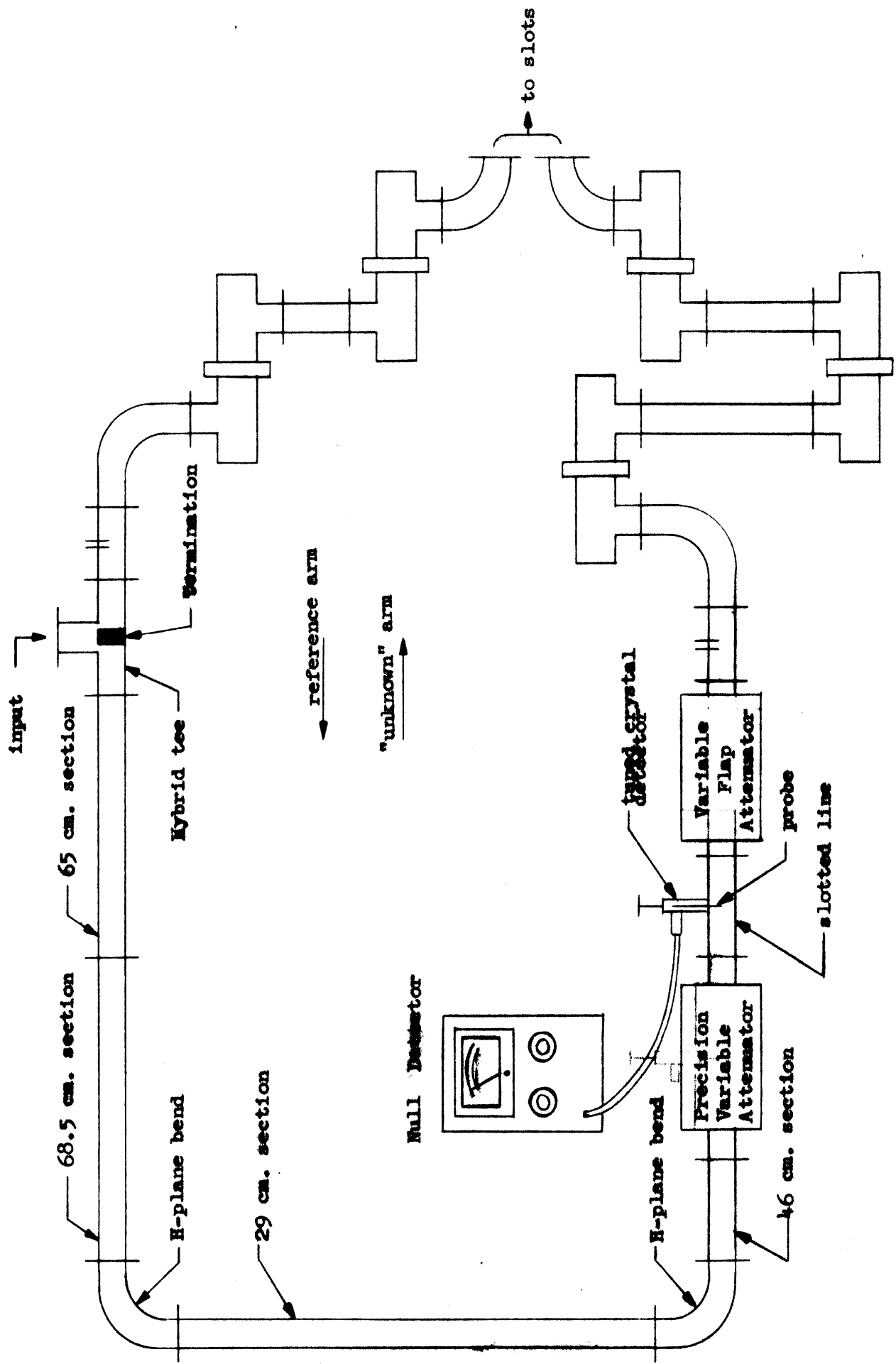


Figure 18. Final Layout of Revised Microwave Bridge

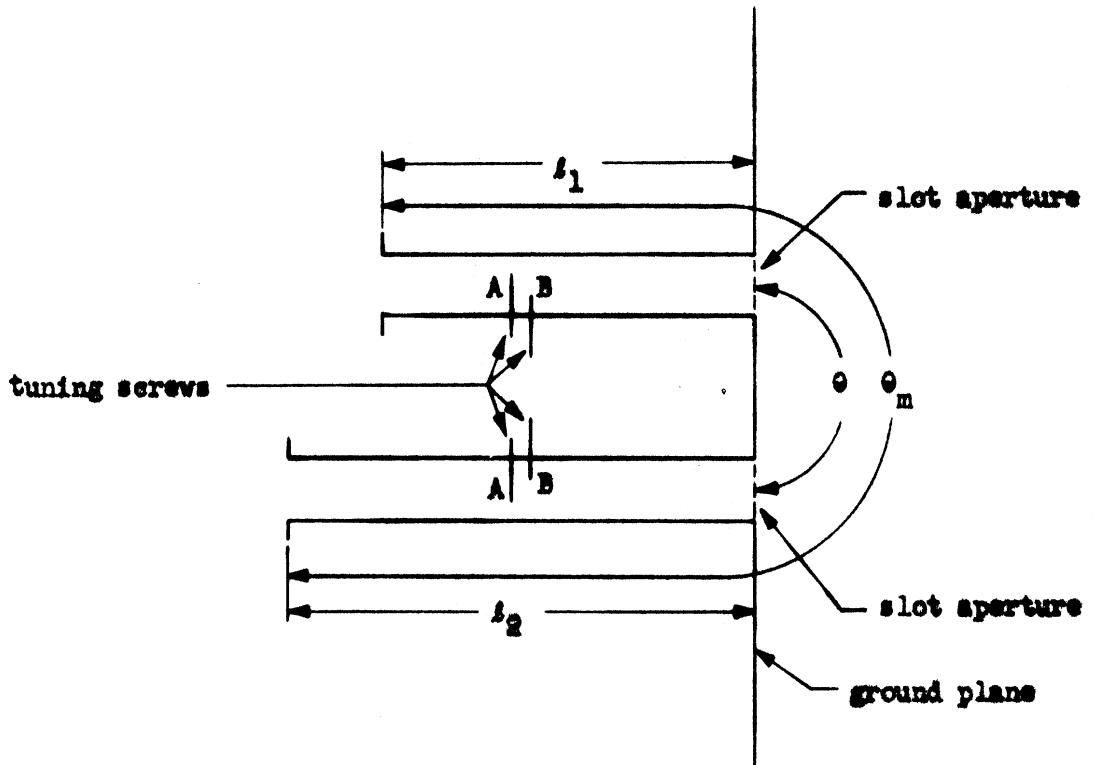


Figure 19. Slot Coupling Phase Relationships

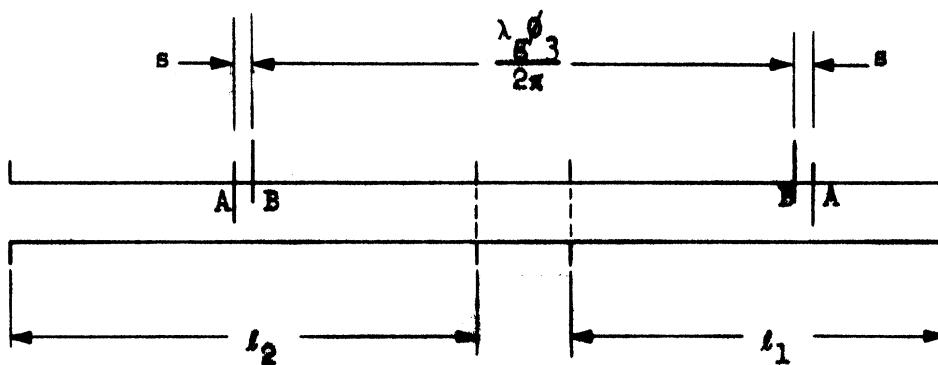


Figure 20. Slot Waveguide Assembly with Tuned Screws

mounted on the ground plane. The two waveguides are then carefully removed from the ground plane and equipped with flanges. Because each set of tuning screws is mounted a fixed distance from the ground plane for coupling measurements, and because the separation between the two screws is the same for all slot waveguides, it is assumed that all sets of tuning screws are adjusted to the same tuning. Hence, each of the two waveguides removed include a representative set of tuned screws.

From the Smith diagram (Figure 21), it can be seen that if the assembly shown in Figure 20 is terminated with a matched load, then only a pure phase shift,  $\phi_3$ , is required between the back-to-back slot waveguides to obtain a match at the input of the assembly. For the sake of clarity, stubs "A" and stubs "B" have been assumed to present normalized shunt susceptances of  $b_A = +1.0$  and  $b_B = +2.0$  respectively. The diagram is obtained by assuming a perfect match at both input and output terminals, and plotting the admittance of each half of the assembly while moving toward the short section in the center. The short section then provides the required phase shift ( $\phi_3$ ) to join the two end points on the diagram. Note that it is not necessary to preserve lengths  $l_1$  and  $l_2$  after removing the slot waveguides from the ground plane; it is only necessary to preserve the tuning of the two sets of screws. A change in  $l_1$  and/or  $l_2$  may simply require a different value of  $\phi_3$  to produce a match, and  $\phi$  is independent of  $\phi_3$ .

To actually produce this condition in the laboratory, the assembly was terminated with a perfectly matched load consisting of a typical lossy termination plus a double-stub tuner adjusted to cancel the residual reflection at the frequency of operation. The straight section in the center of the assembly was progressively machined to smaller lengths and the input VSWR of the assembly was measured and plotted as a function of the electrical length of the straight

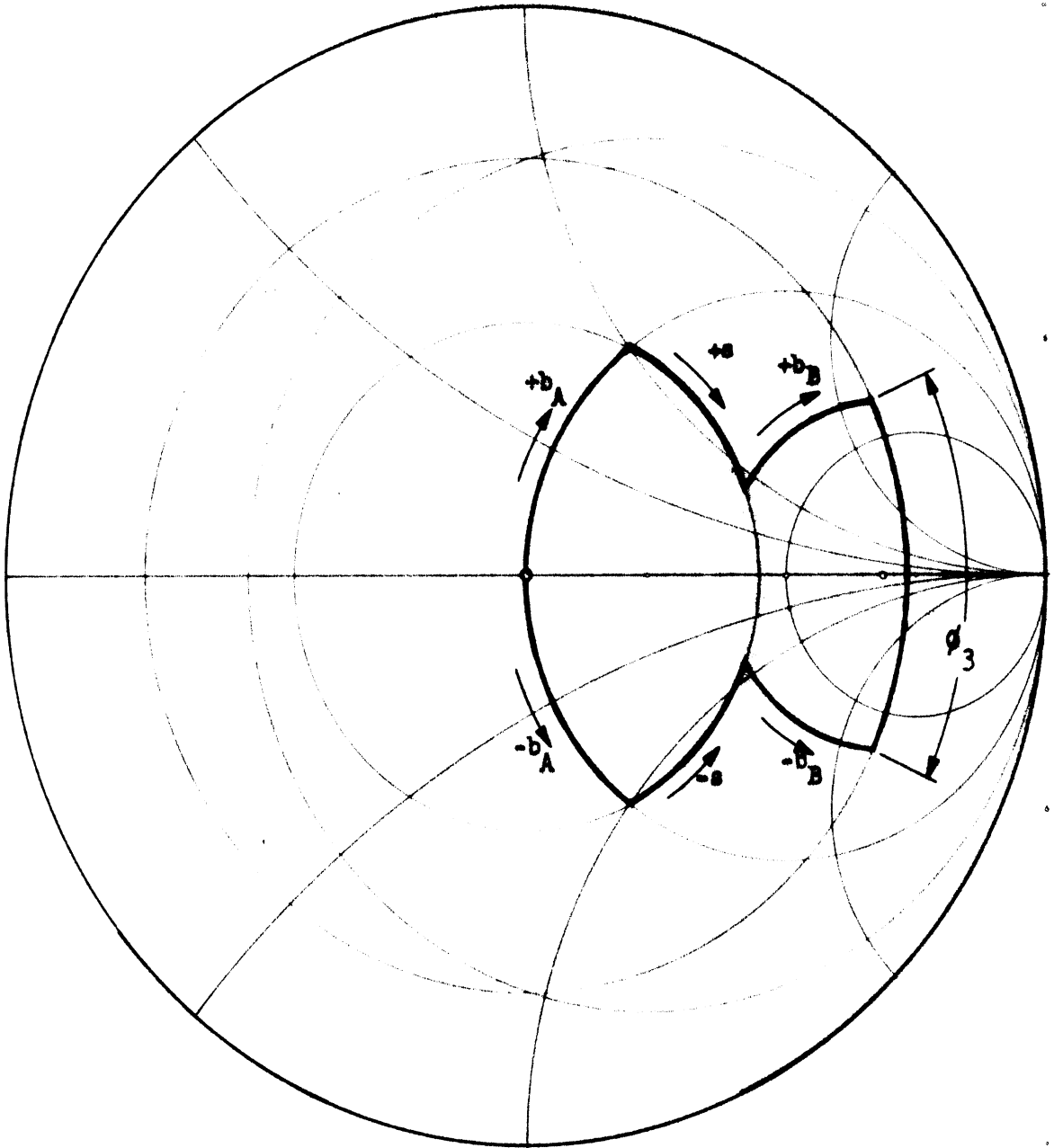


Figure 21. Smith Diagram for Slot Waveguide Assembly

section (see Figure 22). A second waveguide section was then machined to the optimum length and connected into the assembly. The phase shift through this assembly can now be measured with the microwave bridge. To obtain the phase shift introduced by two sets of tuning screws ( $2\phi$ ), it is only necessary to remove the screws after having obtained the previous measurement and again measure the phase shift through the assembly. The difference in the phase shift, introduced by the removal of the screws, is equal to minus  $2\phi$ .

Returning to the original problem, that of obtaining  $\theta$  from  $\theta_m$  (Equation (33)), it can be seen that the two remaining factors to be determined are  $\phi_1$  and  $\phi_2$ . These phase shifts can be determined, with the slot waveguides involved mounted on the ground plane, by the method of Section 4.2.1.9. It is necessary to temporarily remove the tuning screws to make these measurements.

4.2.2. WAVEGUIDE-TO-MONOPOLE TRANSFORMER CHARACTERISTICS. Results of measurements on the monopole feed system are illustrated in Figures 23 and 24. Two areas were explored:

- a. The input VSWR of the ridge transformer was determined across a frequency band, first with the short adjusted for the best match at 2.81 kmc., and second with the short adjusted for an optimum match at each frequency.
- b. For various monopole lengths, that frequency was found which gave the best match while varying the short position.

4.2.2.1. Input VSWR Across a Frequency Band. All the monopoles used had hemispherical end caps. For frequencies lying between 2750 and 2870 mcs. the VSWR was measured for the ridge transformer loaded with a short and a monopole of length  $h = .9600$  inch ( $2h/\lambda = .4571$  at 2810 mcs., the calculated resonance).

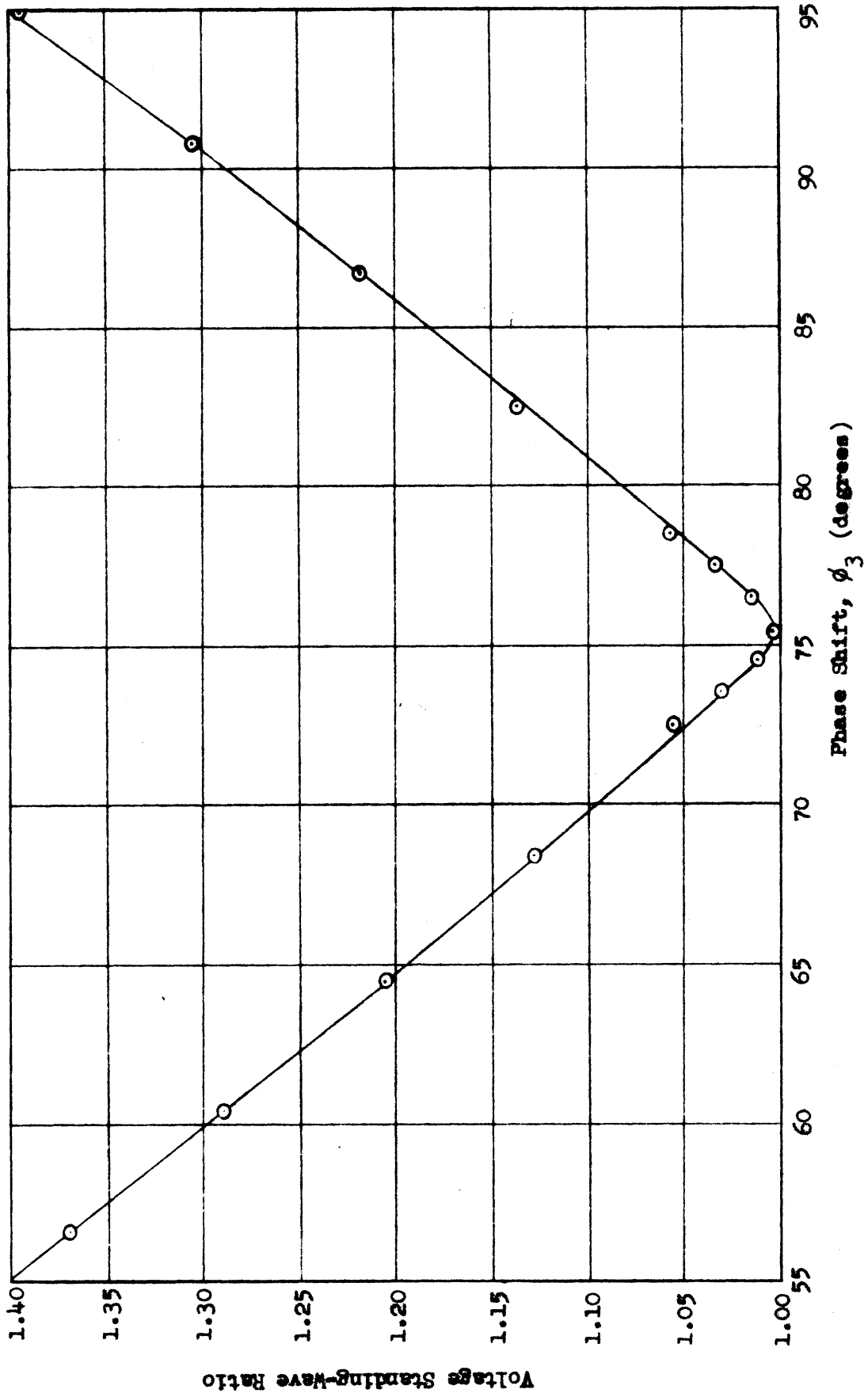
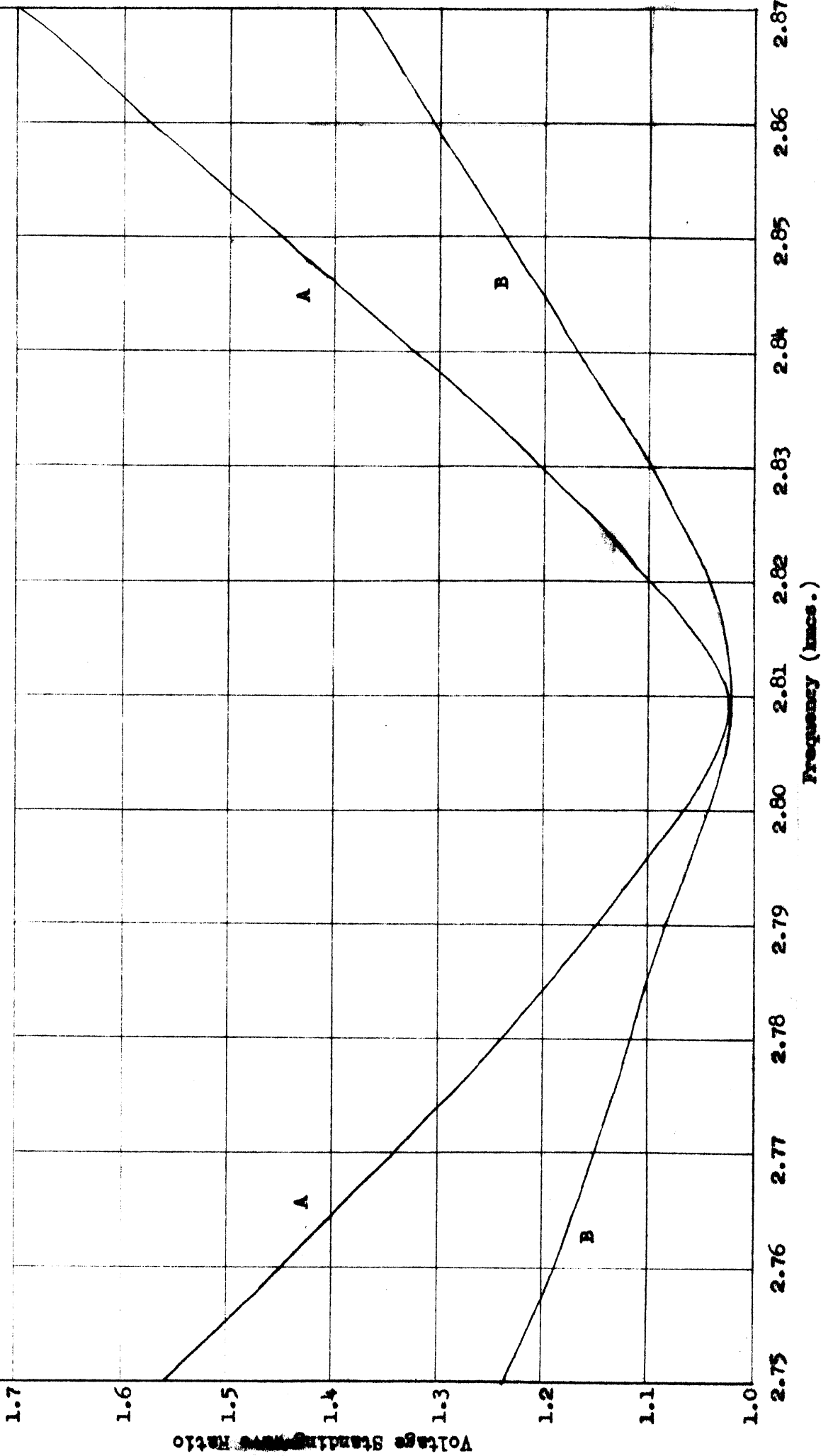


Figure 22. VSWR of Slot Waveguide Assembly versus Phase Shift of Short Section

Figure 23. VSWR of Waveguide-to-Monopole Transformer Loaded with Monopole (resonant at 2.81 mcs.)

A - no adjustment

B - returned short





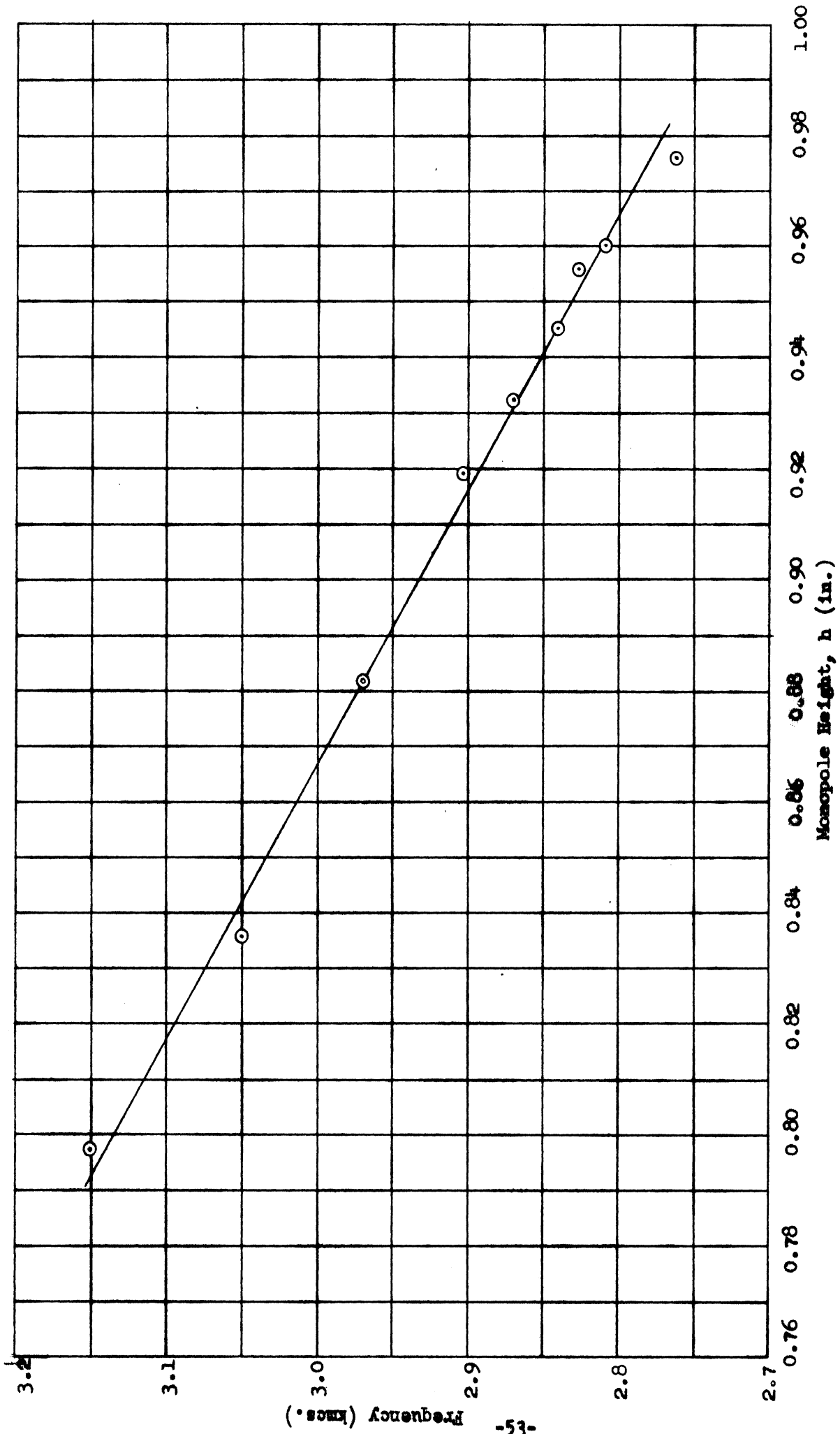


Figure 24. Optimum Frequency versus Monopole Height

The ridge impedance at the junction point with the monopole is 33.83 ohms. This ridge impedance corresponds to a clearance of .090 inch between the top of the ridge and the top wall of S-band waveguide (2.841" x 1.345" I.D.). Of the two curves shown in Figure 23, curve A was obtained by adjusting the short (terminating the ridge waveguide) for minimum VSWR at the resonant frequency of the monopole, i.e., at 2810 mcs., and then taking the remainder of the data by changing only the frequency. For curve B the position of the short was adjusted at each frequency to yield the minimum VSWR obtainable. The difference in broad-band operating characteristics is quite noticeable: For curve A, there is a 1.64-percent (46 mcs.) bandwidth across which the VSWR is less than 1.2. By retuning the short for each frequency, a bandwidth of 3.12 percent (88 mcs.) is obtained for the same VSWR, as shown by curve B. One interesting point to be derived from the VSWR curves is this: Assuming a center frequency of 2.81 kmcs., a  $\pm$  30 mcs. drift in frequency can be tolerated before the radiated power will be down more 0.1 db due to mismatch. Of course this number will have to be doubled to account for a similar mismatch on the receiving end of the system.

#### 4.2.2.2. Minimum VSWR vs. Frequency for Different Lengths of Monopoles.

Antenna lengths between 0.7970 inch and .9760 inch were inserted as radiating elements into the ridge-transformer monopole mount. For each antenna a frequency was determined at which, by varying the position of the ridge-guide short, the VSWR could be minimized. The radius of each monopole was .045 inch. Figure 24 shows the experimental curve of frequency versus monopole length. For each antenna the minimum VSWR obtained was less than 1.03.

APPENDIX

Calculation of Equation (21)

The integral part of Equation (21) is denoted by K, namely

$$K = \int_{-\frac{a}{2}}^{\frac{a}{2}} dx \int_{-\frac{b}{2}}^{\frac{b}{2}} dy \int_{-\frac{a}{2}}^{\frac{a}{2}} dx' \int_{-\frac{b}{2}}^{\frac{b}{2}} dy' \hat{y}_0 \cos \frac{\pi y}{b} \cdot \left( \hat{I} + \frac{\nabla \nabla}{k^2} \right) \cdot \hat{y}_0$$

$$\frac{e^{+jk|\vec{r} - \vec{r}'|}}{|\vec{r} - \vec{r}'|} \cos \frac{\pi y'}{b}$$

since  $\vec{r}$  and  $\vec{r}'$  are on the same transmitting slot and  $z = z' = \text{zero}$ , hence;

$$K = \iiint \cos \frac{\pi y}{b} \cos \frac{\pi y'}{b} \left( 1 + \frac{1}{k^2} \frac{\partial^2}{\partial y^2} \right) \frac{e^{+jkR}}{R} dx dy dx' dy'$$

where  $R = \sqrt{(x - x')^2 + (y - y')^2}$

Since  $\frac{\partial^2}{\partial y^2} \left( \frac{e^{-jk|\vec{r} - \vec{r}'|}}{|\vec{r} - \vec{r}'|} \right) = - \frac{\partial^2}{\partial y \partial y'} \left( \frac{e^{-jk|\vec{r} - \vec{r}'|}}{|\vec{r} - \vec{r}'|} \right)$ ,

$$K = \iiint \cos \frac{\pi y}{b} \cos \frac{\pi y'}{b} \frac{e^{+jkR}}{R} dx dy dx' dy'$$

$$- \frac{1}{k^2} \iiint \cos \frac{\pi y}{b} \cos \frac{\pi y'}{b} \frac{\partial}{\partial y} \frac{\partial}{\partial y'} \frac{e^{+jkR}}{R} dx dy dx' dy'$$

The differentiation involved in the above formula can be removed by integration by parts, for instance in the integral,

$$I = \int_{-\frac{b}{2}}^{\frac{b}{2}} dy \int_{-\frac{b}{2}}^{\frac{b}{2}} dy' \cos \frac{\pi y}{b} \cos \frac{\pi y'}{b} \frac{\partial}{\partial y} \frac{\partial}{\partial y'} \frac{e^{+jkR}}{R}$$

Consider only the integration with  $y'$ , and let  $u = \cos \frac{\pi y'}{b}$  and  $dv = \frac{\partial}{\partial y'} \frac{e^{+jkR}}{R} dy'$ ;

then

$$I = \int_{-\frac{b}{2}}^{\frac{b}{2}} dy \cos \frac{\pi y}{b} \left[ \left( \cos \frac{\pi y'}{b} \right) \frac{\partial}{\partial y'} \frac{e^{+jkR}}{R} \right]_{y' = -\frac{b}{2}}^{y' = \frac{b}{2}} + \frac{\pi}{b} \int_{-\frac{b}{2}}^{\frac{b}{2}} dy' \left( \sin \frac{\pi y'}{b} \right) \frac{\partial}{\partial y} \frac{e^{+jkR}}{R}$$

$$I = \frac{\pi}{b} \int_{-\frac{b}{2}}^{\frac{b}{2}} dy \cos \frac{\pi y}{b} \int_{-\frac{b}{2}}^{\frac{b}{2}} dy' \sin \frac{\pi y'}{b} \frac{\partial}{\partial y} \frac{e^{+jkR}}{R}$$

$$I = \frac{\pi}{b} \int_{-\frac{b}{2}}^{\frac{b}{2}} dy' \sin \frac{\pi y'}{b} \int_{-\frac{b}{2}}^{\frac{b}{2}} dy \cos \frac{\pi y}{b} \frac{\partial}{\partial y} \frac{e^{+jkR}}{R}$$

Now consider the integration with respect to  $y$  and similarly perform the integration by parts as that done for  $y'$ . Hence,

$$I = \frac{\pi}{b} \int_{-\frac{b}{2}}^{\frac{b}{2}} dy' \sin \frac{\pi y'}{b} \left[ \left( \cos \frac{\pi y}{b} \right) \frac{e^{+jkR}}{R} \right]_{y = -\frac{b}{2}}^{y = \frac{b}{2}} + \frac{\pi}{b} \int_{-\frac{b}{2}}^{\frac{b}{2}} dy' \left( \sin \frac{\pi y}{b} \right) \frac{e^{+jkR}}{R}$$

$$I = \left( \frac{\pi}{b} \right)^2 \int_{-\frac{b}{2}}^{\frac{b}{2}} dy \int_{-\frac{b}{2}}^{\frac{b}{2}} dy' \left( \sin \frac{\pi y}{b} \right) \left( \sin \frac{\pi y'}{b} \right) \frac{e^{+jkR}}{R}$$

Therefore

$$\begin{aligned}
 K &= \iiint \left( \cos \frac{\pi y}{b} \right) \left( \cos \frac{\pi y'}{b} \right) \frac{e^{+jkR}}{R} dx dy dx' dy' \\
 &\quad - \frac{1}{k^2} \left( \frac{\pi}{b} \right)^2 \iiint \left( \sin \frac{\pi y}{b} \right) \left( \sin \frac{\pi y'}{b} \right) \frac{e^{+jkR}}{R} dx dy dx' dy' \\
 K &= \frac{1}{2} \iiint \left[ \cos \frac{\pi}{b} (y + y') + \cos \frac{\pi}{b} (y - y') \right] \frac{e^{+jkR}}{R} dx dy dx' dy' \\
 &\quad + \frac{1}{2} \frac{1}{k^2} \left( \frac{\pi}{b} \right)^2 \iiint \left[ \cos \frac{\pi}{b} (y + y') - \cos \frac{\pi}{b} (y - y') \right] \frac{e^{+jkR}}{R} dx dy dx' dy'
 \end{aligned}$$

Now introduce new integration variables:

$$\begin{aligned}
 \frac{\pi}{b} (y + y') &= \mu & \frac{\pi}{b} (y - y') &= \lambda \\
 \frac{\pi}{b} (x + x') &= \nu & \frac{\pi}{b} (x - x') &= \sigma
 \end{aligned}$$

Then

$$dy dy' = \left| J \begin{pmatrix} y, y' \\ \mu, \lambda \end{pmatrix} \right| d\mu d\lambda = \frac{1}{2} \left( \frac{b}{\pi} \right)^2 d\mu d\lambda,$$

where

$$J \begin{pmatrix} y, y' \\ \mu, \lambda \end{pmatrix} = \begin{vmatrix} \frac{\partial y}{\partial \mu} & \frac{\partial y'}{\partial \mu} \\ \frac{\partial y}{\partial \lambda} & \frac{\partial y'}{\partial \lambda} \end{vmatrix} = \begin{vmatrix} \frac{b}{2\pi} & \frac{b}{2\pi} \\ \frac{b}{2\pi} & -\frac{b}{2\pi} \end{vmatrix} = -\frac{1}{2} \left( \frac{b}{\pi} \right)^2$$

$$\text{Similarly } dx dx' = \frac{1}{2} \left( \frac{b}{\pi} \right)^2 d\nu d\sigma.$$

The ranges of integration are shown in Figures 25 and 26.

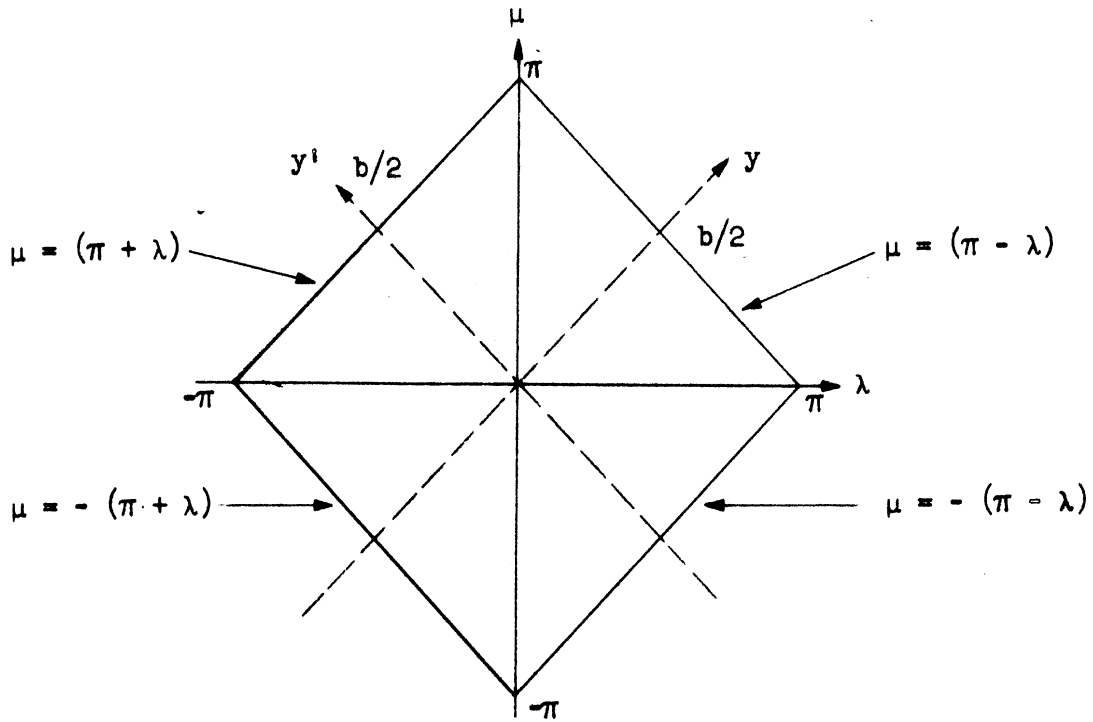


Figure 25. Range of Integration for  $\mu$  and  $\lambda$

When  $\lambda$  goes from 0 to  $\pi$ ,  $\mu$  ranges from  $-(\pi - \lambda)$  to  $(\pi - \lambda)$ . When  $\lambda$  goes from  $-\pi$  to 0,  $\mu$  ranges from  $-(\pi + \lambda)$  to  $(\pi + \lambda)$ .

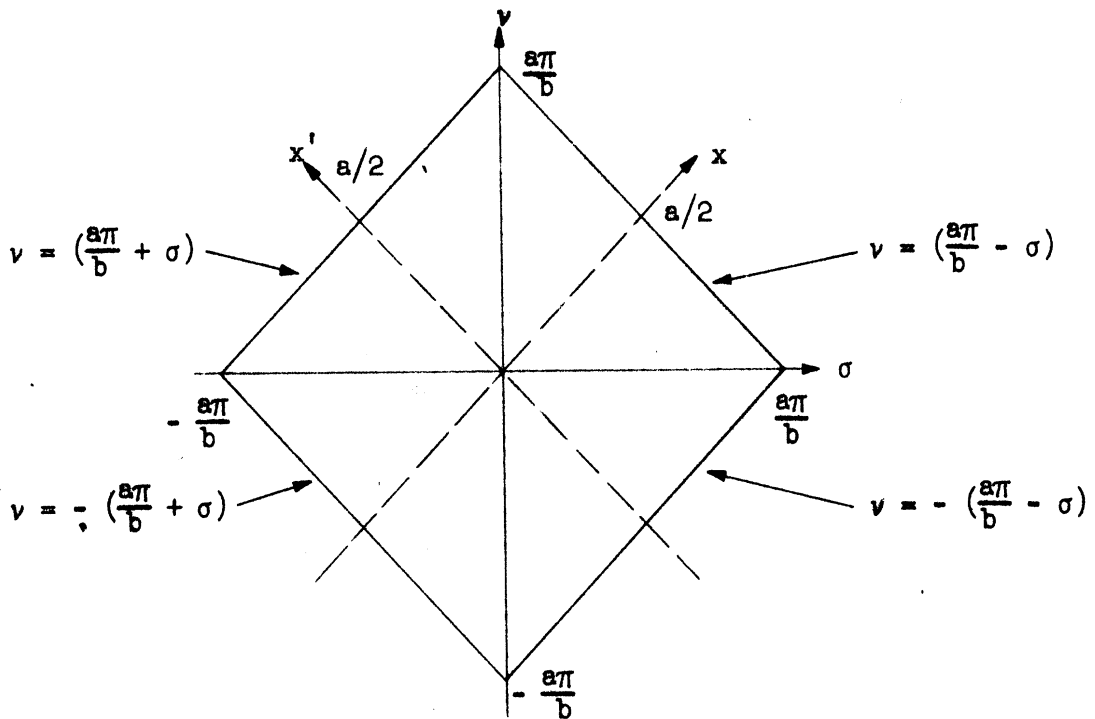


Figure 26. Range of Integration for  $\nu$  and  $\sigma$

When  $\sigma$  goes from 0 to  $\frac{a\pi}{b}$ ,  $\nu$  ranges from  $-\left(\frac{a\pi}{b} - \sigma\right)$  to  $\left(\frac{a\pi}{b} - \sigma\right)$ . When  $\sigma$  goes from  $-\frac{a\pi}{b}$  to 0,  $\nu$  ranges from  $-\left(\frac{a\pi}{b} + \sigma\right)$  to  $\left(\frac{a\pi}{b} + \sigma\right)$ . Let

$A = \sqrt{\lambda^2 + \sigma^2}$ , then let  $f(A) = \frac{1}{A} \exp(jk b A / \pi)$ ; then

$$K = \frac{1}{8} \left(\frac{b}{\pi}\right)^4 \iiint \left[ \cos \mu + \cos \lambda \right] f(A) d\mu d\lambda d\nu d\sigma$$

$$+ \frac{1}{8} \frac{1}{k^2} \iiint \left[ \cos \mu - \cos \lambda \right] \frac{\pi}{b} f(A) d\mu d\lambda d\nu d\sigma$$

Due to the symmetry of the integrand, the integrations can be carried out for one quadrant in both Figure 25 and Figure 26. The final result is obtained by multiplying the quadruple integral by sixteen.

$$K = 2 \left(\frac{b}{\pi}\right)^4 \left(\frac{\pi}{b}\right) \int_0^{\pi-\lambda} d\mu \int_0^{\pi} d\lambda \int_0^{\frac{a\pi}{b}-\sigma} d\nu \int_0^{\frac{a\pi}{b}} d\sigma \left[ \cos \mu + \cos \lambda \right] f(A)$$

$$= 2 \left(\frac{b}{\pi}\right)^2 \left(\frac{\pi}{b}\right) \frac{1}{k^2} \int_0^{\pi-\lambda} d\mu \int_0^{\pi} d\lambda \int_0^{\frac{a\pi}{b}-\sigma} d\nu \int_0^{\frac{a\pi}{b}} d\sigma \left[ \cos \mu - \cos \lambda \right] f(A)$$

First integrate with respect to  $\mu$  and  $\nu$ :

$$K = 2 \left(\frac{b}{\pi}\right)^3 \left\{ \int_0^{\frac{a\pi}{b}} d\sigma \left(\frac{a\pi}{b} - \sigma\right) \int_0^{\pi} d\lambda \left[ \sin \lambda + (\pi-\lambda) \cos \lambda \right] f(A) \right.$$

$$\left. + \frac{1}{k^2} \left(\frac{\pi}{b}\right)^2 \int_0^{\frac{a\pi}{b}} d\sigma \left(\frac{a\pi}{b} - \sigma\right) \int_0^{\pi} d\lambda \left[ \sin \lambda - (\pi-\lambda) \cos \lambda \right] f(A) \right\}$$

Rearranging the terms,

$$K = \frac{2b\pi}{k^2} \left\{ \left[ \left( \frac{kb}{\pi} \right)^2 - 1 \right] \int_0^{\frac{a\pi}{b}} d\sigma \left( \frac{a}{b} - \frac{\sigma}{\pi} \right) \int_0^{\pi} d\lambda \left( 1 - \frac{\lambda}{\pi} \right) \cos \lambda f(A) \right. \\ \left. + \frac{1}{\pi} \left[ \left( \frac{kb}{\pi} \right)^2 + 1 \right] \int_0^{\frac{a\pi}{b}} d\sigma \left( \frac{a}{b} - \frac{\sigma}{\pi} \right) \int_0^{\pi} d\lambda f(A) \sin \lambda \right\}$$

Equation (21) then states

$$W = \frac{1}{2} \operatorname{Re} \frac{-j\omega\epsilon}{2\pi} E_o^2 K \\ = \frac{\omega\epsilon b}{2k^2} \left\{ \left[ \left( \frac{kb}{\pi} \right)^2 - 1 \right] \int_0^{\frac{a\pi}{b}} d\sigma \left( \frac{a}{b} - \frac{\sigma}{\pi} \right) \int_0^{\pi} d\lambda \left( 1 - \frac{\lambda}{\pi} \right) \frac{\cos \lambda \sin \left( \frac{kb}{\pi} A \right)}{A} \right. \\ \left. + \left[ \left( \frac{kb}{\pi} \right)^2 + 1 \right] \int_0^{\frac{a\pi}{b}} d\sigma \left( \frac{a}{b} - \frac{\sigma}{\pi} \right) \int_0^{\pi} d\lambda \frac{\sin \lambda \sin \left( \frac{kb}{\pi} A \right)}{\pi A} \right\}$$

Now use the following approximation:

$$\frac{\sin \left( \frac{kb}{\pi} A \right)}{A} = \frac{\sin \frac{kb}{\pi} \sqrt{\lambda^2 + \sigma^2}}{\sqrt{\lambda^2 + \sigma^2}} = \frac{kb}{\pi} - \frac{\left( \frac{kb}{\pi} \right)^3 (\lambda^2 + \sigma^2)}{6} + \frac{\left( \frac{kb}{\pi} \right)^5 (\lambda^2 + \sigma^2)^2}{120} \\ - \frac{\left( \frac{kb}{\pi} \right)^7 (\lambda^2 + \sigma^2)^3}{5040} + \dots$$



Substituting this approximation into the above formula, perform the straightforward integration.

$$\begin{aligned}
 W = & \frac{\omega \epsilon b}{k^2} \left(\frac{kb}{\pi}\right)^2 \left(\frac{kb}{\pi}\right) \frac{a}{b} \frac{2}{3} \left\{ 1 - \left[ \frac{3}{15} (\pi^2 - 8) \left(\frac{b}{\lambda}\right)^2 + \frac{2\pi^2}{15} \left(\frac{a}{\lambda}\right)^2 \right] \right. \\
 & + \left[ \frac{1}{105} (3\pi^4 - 72\pi^2 + 432) \left(\frac{b}{\lambda}\right)^4 + \frac{2\pi^2}{105} (\pi^2 - 8) \left(\frac{ab}{\lambda^2}\right)^2 + \frac{3\pi^4}{525} \left(\frac{a}{\lambda}\right)^4 \right] \\
 & - \left[ \frac{1}{105} (\pi^6 - 60\pi^4 + 1080\pi^2 - 5760) \left(\frac{b}{\lambda}\right)^6 \right. \\
 & \left. \left. + \frac{\pi^2}{210} (\pi^4 - 24\pi^2 + 144) \left(\frac{ab^2}{\lambda^3}\right)^2 + \dots \right] + \dots \right\}
 \end{aligned}$$

or

$$\begin{aligned}
 W = & \frac{8}{3\pi} \sqrt{\frac{\epsilon}{\mu}} \left(\frac{ab}{\lambda}\right)^2 \left\{ 1 - \frac{3}{15} (\pi^2 - 8) \left(\frac{b}{\lambda}\right)^2 + \frac{1}{105} (3\pi^4 - 72\pi^2 + 432) \left(\frac{b}{\lambda}\right)^4 \right. \\
 & - \frac{1}{105} (\pi^6 - 60\pi^4 + 1080\pi^2 - 5760) \left(\frac{b}{\lambda}\right)^6 \\
 & - \frac{2\pi^2}{15} \left(\frac{a}{\lambda}\right)^2 \left[ 1 - \frac{1}{7} (\pi^2 - 8) \left(\frac{b}{\lambda}\right)^2 + \frac{1}{28} (\pi^4 - 24\pi^2 + 144) \left(\frac{b}{\lambda}\right)^4 \right] \\
 & \left. + \frac{3\pi^4}{525} \left(\frac{a}{\lambda}\right)^4 + \dots \right\}
 \end{aligned}$$

## REFERENCES

1. J. A. Stratton, Electromagnetic Theory, McGraw Hill, New York, 1941, p. 29.
2. J. A. Stratton, Electromagnetic Theory, McGraw Hill, New York, 1941, p. 431.
3. L. Lewin, Advanced Theory of Wave Guides, Ilissee and Sons, London, 1951, p. 123.
4. N. Marcuvitz and L. B. Felsen, "Slot Coupling of Rectangular and Spherical Waveguides", *Journal of Applied Physics*, Vol. 24, No. 2, June 1953, p. 755.
5. E. M. Turner, "Spiral Slot Antenna", Technical Note WCLR-55-8, Wright Air Development Center, Dayton, Ohio, June 1955.
6. R. Bawer and J. J. Wolfe, "The Spiral Antenna", Institute of Radio Engineers, International Convention Record, Part 1, 1960.
7. J. A. Kaiser, "The Archimedean Two-Wire Spiral Antenna", Institute of Radio Engineers, Professional Group on Antennas and Propagation, May 1960.
8. B. M. Schiffman, "A New Class of Broad-Band Microwave 90-Degree Phase Shifters", Institute of Radio Engineers, Professional Group on Microwave Theory and Techniques, April 1958.
9. J. H. Craven, "A Novel Broad-Band Balun", Institute of Radio Engineers, Professional Group on Microwave Theory and Techniques, November 1960.